nature cell biology

Microtubule minus-end regulation at spindle poles by an ASPM–katanin complex

Kai Jiang[1,4,5], Lenka Rezabkova[2,4], Shasha Hua[1], Qingyang Liu[1], Guido Capitani[2], A. F. Maarten Altelaar[3], Albert J. R. Heck[3], Richard A. Kammerer[2,5], Michel O. Steinmetz[2,5] and Anna Akhmanova[1,5]

ASPM (known as Asp in fly and ASPM-1 in worm) is a microcephaly-associated protein family that regulates spindle architecture, but the underlying mechanism is poorly understood. Here, we show that ASPM forms a complex with another protein linked to microcephaly, the microtubule-severing ATPase katanin. ASPM and katanin localize to spindle poles in a mutually dependent manner and regulate spindle flux. X-ray crystallography revealed that the heterodimer formed by the N- and C-terminal domains of the katanin subunits p60 and p80, respectively, binds conserved motifs in ASPM. Reconstitution experiments demonstrated that ASPM autonomously tracks growing microtubule minus ends and inhibits their growth, while katanin decorates and bends both ends of dynamic microtubules and potentiates the minus-end blocking activity of ASPM. ASPM also binds along microtubules, recruits katanin and promotes katanin-mediated severing of dynamic microtubules. We propose that the ASPM–katanin complex controls microtubule disassembly at spindle poles and that misregulation of this process can lead to microcephaly.

Microcephaly is a neurodevelopmental disorder characterized by small brain and mental retardation. A significant number of proteins implicated in microcephaly, including ASPM (abnormal spindle-like microcephaly associated) participate in organizing mitotic spindle poles[1]. The function of a spindle pole depends on microtubule nucleation as well as stabilization, disassembly and bundling of microtubule minus ends. Microtubule minus ends can grow and shrink *in vitro*[2]; however, it is generally believed that within mitotic spindles, minus ends are either stable or slowly depolymerize, resulting in poleward microtubule flux[3]. The molecular mechanisms controlling microtubule minus-end behaviour in the spindle are poorly understood.

Previous work indicated that ASPM (known as Asp in fly and ASPM-1 in worm) is an excellent candidate for being a mitotic microtubule minus-end regulator[4–13]. It is encoded by the gene that is most frequently mutated in microcephaly[14], but the molecular mechanism underlying ASPM activity is not understood. Katanin, a conserved microtubule-severing protein complex, which consists of the AAA ATPase containing enzymatic subunit p60 and the regulatory subunit p80[15–17], is also linked to microcephaly[18,19]. Formation of the katanin p60/p80 heterodimer is mediated by the N-terminal microtubule interacting and trafficking domain of p60 and a conserved C-terminal domain of p80 (ref. 20). Katanin localizes to spindle poles during mitosis in most animal cells and plays an important role in spindle organization[18,19,21–25]. Mutations in the katanin-encoding gene in microcephaly patients lead to a dramatic increase of centrosome numbers and multipolar spindles, suggesting a role in preventing centriole overduplication[19].

Most of the past *in vitro* work on katanin focused on the p60 subunit using stable microtubules as a substrate. Importantly, the severing activity of p60 is strongly suppressed by free tubulin[26], suggesting that additional factors are needed for katanin-mediated microtubule severing in cells. Here, we show that ASPM forms a physiological complex with katanin p60/80 and promotes its activity. Through a combination of structural analysis, genome editing in cells, *in vitro* reconstitution assays and live cell imaging, we demonstrate that the ASPM–katanin complex probably acts through a combination of microtubule-severing and minus-end blocking activities and regulates spindle flux. Our data thus identify the ASPM–katanin complex as a microtubule minus-end regulator and suggest that its perturbation might lead to neurodevelopmental disease.

RESULTS

ASPM and katanin form a complex and regulate spindle flux

To gain insight into the function of ASPM, we tagged the endogenous protein with a strep tag and green fluorescent protein (GFP) by

[1]Cell Biology, Department of Biology, Faculty of Science, Utrecht University, Padualaan 8, 3584 CH Utrecht, The Netherlands. [2]Laboratory of Biomolecular Research, Division of Biology and Chemistry, Paul Scherrer Institut, 5232 Villigen PSI, Switzerland. [3]Biomolecular Mass Spectrometry and Proteomics, Bijvoet Center for Biomolecular Research, Utrecht Institute for Pharmaceutical Sciences and The Netherlands Proteomics Centre, Utrecht University, Padualaan 8, 3584 CH Utrecht, The Netherlands. [4]These authors contributed equally to this work.
[5]Correspondence should be addressed to K.J., R.A.K., M.O.S. or A.A.
(e-mail: k.jiang@uu.nl or richard.kammerer@psi.ch or michel.steinmetz@psi.ch or a.akhmanova@uu.nl)

Received 13 September 2016; accepted 15 March 2017; published online 24 April 2017; corrected after print 22 May 2017; DOI: 10.1038/ncb3511

a

Accession	Name	Score	Coverage (%)	Total peptides
Q8IZT6	ASPM	2,836.05	17.26	111
P62158	Calmodulin	304.24	46.98	9
O75449	Katanin p60	120.88	16.70	8
Q9BVA0	Katanin p80	67.94	2.60	1

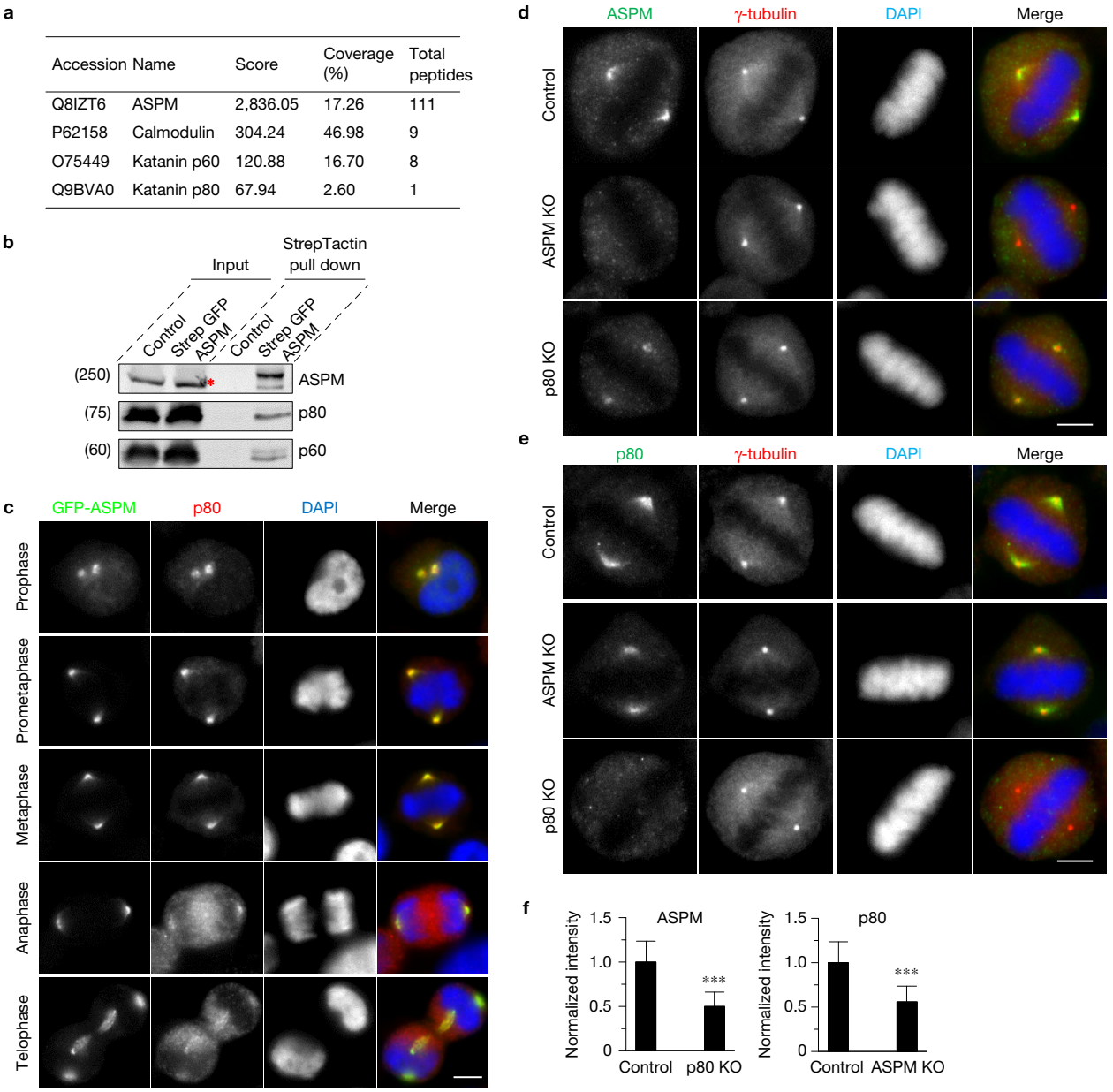

Figure 1 ASPM and katanin form a complex at spindle poles. (**a**) Mass spectrometry results of StrepTactin pull down from strep-GFP-ASPM knock-in HEK293T cells synchronized in mitosis (see Supplementary Table 2 for a complete list of specific hits). 16 out of 111 peptides of ASPM are unique to the long isoform, although only the short isoform could be detected by western blotting in **b**. (**b**) StrepTactin pull down assay with lysates of strep-GFP-ASPM knock-in HEK293T cells. The red asterisk indicates a non-specific band detected by ASPM antibody in cell extract, overlapping with the specific band visible in the pull down. See Supplementary Fig. 2a for the demonstration of the specificity of anti-katanin antibodies. (**c**) Immunostaining for p80 and DNA (DAPI) in GFP-ASPM knock-in HeLa cells during mitosis. Scale bar, 5 μm. (**d–f**) Immunofluorescence staining and quantification of ASPM and p80 intensities at spindle poles in control or the indicated knockout HeLa cells. For ASPM intensity, $n = 105$ spindle poles, control; $n = 124$, p80 knockout; for p80 intensity, $n = 74$ spindle poles, control; $n = 77$, ASPM knockout. Scale bars, 5 μm. Data represent mean ± s.d. $^{***}P < 0.001$, Mann–Whitney U test. Unprocessed original scans of blots are shown in Supplementary Fig. 8. Source data for **f** can be found in Supplementary Table 5.

CRISPR/Cas9 technology in cultured human cells (Supplementary Fig. 1a and Supplementary Table 1). As expected[5,8], GFP-ASPM localized to spindle poles throughout cell division and to microtubule minus ends of the central spindle during telophase (Supplementary Fig. 1b). To identify potential binding partners of ASPM, we isolated strep-GFP-ASPM and associated proteins from mitotic cells and analysed them by mass spectrometry. In addition to the known partner calmodulin[7,10], this analysis revealed several centrosomal and spindle pole proteins, including the p60 and p80 subunits of katanin (Fig. 1a,b and Supplementary Table 2). The ASPM–katanin interaction is supported by a recent proteomics study of the katanin family[27].

During mitosis, ASPM and katanin co-localize at spindle poles, with the strongest overlap observed from prophase to metaphase

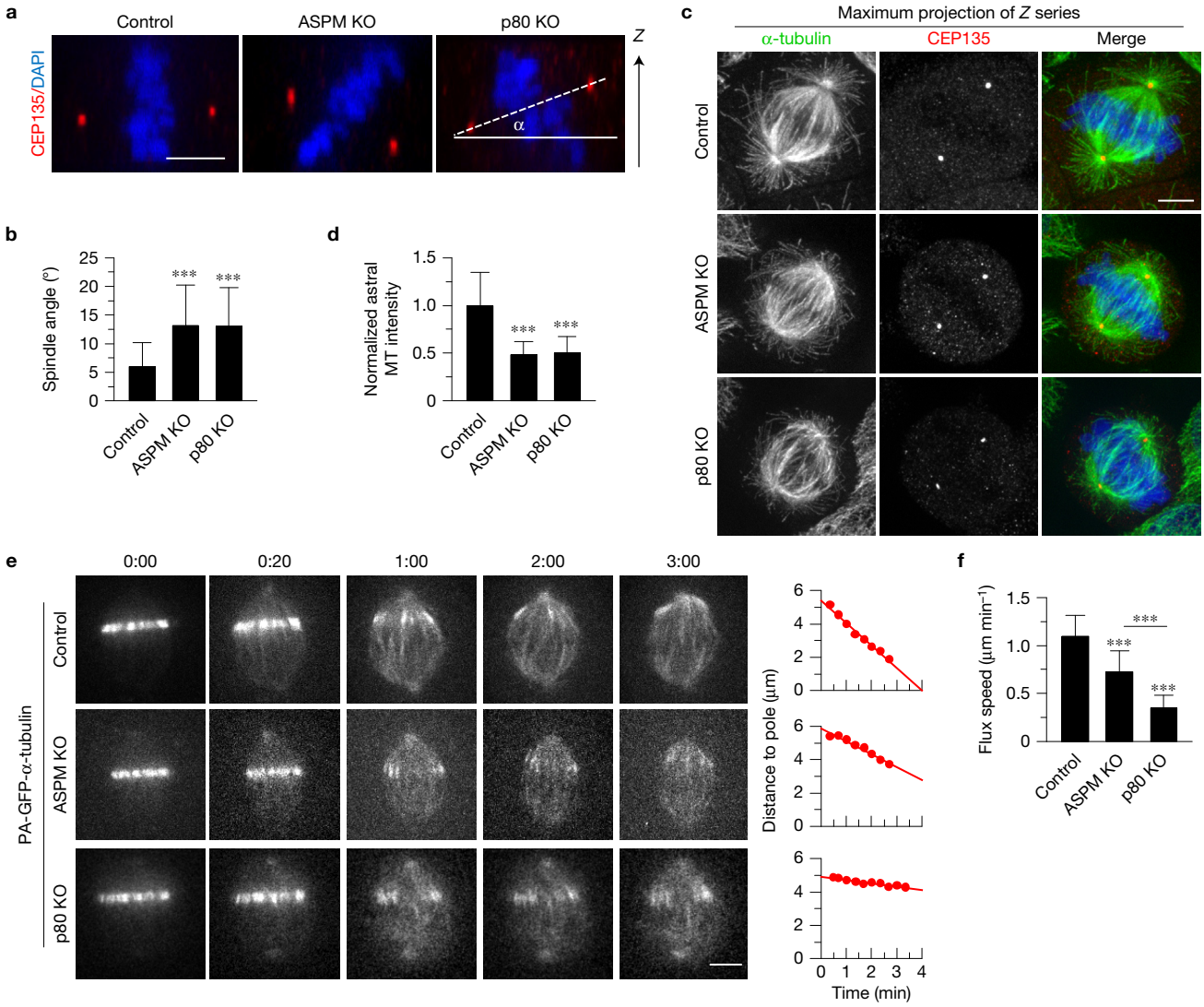

Figure 2 The ASPM–katanin complex regulates spindle orientation and poleward flux. (**a**) Orthogonal view (*x*–*z*) of metaphase HeLa cells stained for CEP135 and DAPI in control, ASPM knockout and p80 knockout HeLa cells. The solid line depicts the horizontal plane; the dashed line indicates the orientation of the spindle with respect to the horizontal plane. Scale bar, 5 μm. (**b**) Quantification of spindle angles as shown in **a**. $n=41$ cells, control; $n=41$, ASPM knockout; $n=39$, p80 knockout. (**c**) Immunostaining for α-tubulin, CEP135 and DNA (DAPI) in control, ASPM knockout and p80 knockout HeLa cells. Maximum intensity projections of *Z* series with ~40 stacks and 200 nm step are shown. Scale bar, 5 μm. (**d**) Quantification of astral microtubule intensity shown in **c**. $n=44$ cells, control; $n=45$, ASPM knockout; $n=40$, p80 knockout. Intensity was normalized to the average intensity in control cells. (**e**) Live cell images of spindle flux in the indicated U2OS cells stably expressing PA-GFP-α-tubulin. Time displayed as min:s. Plots of the distance between photoactivated GFP stripe and the spindle pole over time are shown on the right. The flux speed was derived from the plot slopes (see Methods for details). Scale bar, 5 μm. (**f**) Flux speed in control and knockout cells. $n=26$ cells, control; $n=29$, ASPM knockout; $n=26$, p80 knockout. Data represent mean ± s.d. $^{***}P<0.001$, Mann–Whitney *U* test. Source data for **b**,**d**,**f** can be found in Supplementary Table 5.

(Fig. 1c). Knockouts of ASPM and p80 reduced the localization of each other to spindle poles by ~50% (Fig. 1d–f and Supplementary Fig. 2a,b). This effect was specific, because the spindle pole intensities of two other major spindle pole proteins, NuMA and the dynactin subunit p150^{Glued}, which localize to the minus ends of spindle microtubules[28,29], were largely unaffected upon ASPM and p80 knockout (Supplementary Fig. 2c–e). This result suggests that ASPM and p80 knockouts do not affect the number of microtubule minus ends at spindle poles.

Knockouts of ASPM and p80 showed the previously described spindle defects, such as a strong increase in multipolar spindles in the p80 knockout and spindle misorientation in the ASPM knockout[8,19,30] (Fig. 2a,b and Supplementary Fig. 2f–i). In addition, the knockout of p80 also perturbed spindle orientation (Fig. 2a,b). The spindle misorientation upon ASPM and p80 knockout was probably due to the dramatic reduction of astral microtubules[30] (Fig. 2c,d). Since the knockout of ASPM did not display an increase in multipolar spindles, while both ASPM and p80 knockouts caused spindle orientation defects, these data suggest that the ASPM–katanin complex does not function in restricting centrosome numbers but may regulate spindle pole organization or dynamics.

To address this possibility, we imaged poleward microtubule flux in control, and in ASPM or p80 knockout U2OS cells expressing photoactivatable (PA)-GFP-α-tubulin (Supplementary Fig. 2a,b). The knockout of ASPM and p80 strongly reduced the flux speed in metaphase spindles, with a more severe defect in p80 knockout cells (Fig. 2e,f and Supplementary Video 1). The strong decrease in spindle flux in ASPM and katanin knockout cells did not lead to major changes in spindle length (Supplementary Fig. 2f,h,j), indicating that the reduction in flux might be compensated by altered microtubule dynamics at kinetochores[31,32].

Biochemical characterization of the ASPM–katanin interaction

To gain insight into the functional connection between ASPM and katanin, we investigated their interaction in detail and found that both the p60 and p80 subunits of katanin are required for ASPM binding (Fig. 3a,b). ASPM contains an N-terminal major sperm protein (MSP) domain, a long unstructured region, four calponin homology (CH) domains that can bind microtubules[9], multiple isoleucine-glutamine (IQ) motifs, and a C-terminal HEAT repeat region. Deletion mapping showed that the heterodimer formed between p60N and p80C interacts with ASPM through its unstructured region that contains four conserved peptide repeats (Fig. 3a–e and Supplementary Fig. 3a). Further mapping revealed that the p60N/p80C heterodimer interacted with three out of the four ASPM repeats and preferentially associated with the third repeat (Fig. 3f,g). Sedimentation velocity experiments with purified components verified the direct interaction between p60N/p80C and the third repeat of ASPM and confirmed that this interaction requires both the p60N and p80C subunits (Fig. 3h). These results suggest that the ASPM-binding site on katanin is created upon the formation of the p60N/p80C heterodimer.

Structure of the ASPM–katanin complex

Next, we reconstituted a minimal 1:1:1 stoichiometric complex composed of p60N, p80C and a peptide corresponding to the third repeat of ASPM (ASPMp), and solved the tripartite p60N/p80C/ASPMp complex structure to 1.5 Å resolution by X-ray crystallography (Fig. 4a and Supplementary Table 3). The p60N subunit forms a three-helix bundle, which is consistent with an NMR structure obtained with a shorter version of p60N (ref. 33). The p80C subunit in turn consists of seven helices that adopt an extended helix-turn-helix motif. The interaction between p60N and p80C is mediated by both hydrophobic and polar amino acid residues located in the H1 helix of p80C and helices H1 and H3 of p60N (Fig. 4b). Inspection of the p60N/p80C/ASPMp complex structure in combination with co-immunoprecipitation, sedimentation velocity experiments and circular dichroism spectroscopy suggested that the three microcephaly-associated mutations located within p80C—S538L, L543R and G581D (ref. 18)—affected the stability of the protein, but not its capacity to bind to p60N (Fig. 4c,d and Supplementary Fig. 3b).

In the p60N/p80C/ASPMp complex structure, the ASPMp peptide bound to the site formed at the interface between p60N and p80C, a result that explains why both subunits are needed for tripartite complex formation (Fig. 4a). Residues S351, F352 and L353 of ASPMp were clearly visible in the electron density of the structure (Fig. 4a and Supplementary Fig. 3c). We found that F352 of ASPMp inserts into a hydrophobic pocket formed by L18 and L19 of p60N, and by Y574 of p80C. Individual substitutions of F352 of ASPMp, L18 or L19 of p60N, or Y574 of p80C to alanine abolished the binding between ASPMp and the p60N/p80C heterodimer although they had no effect on the formation and stability of the p60N/p80C heterodimer (Fig. 4c–e). These residues thus have critical roles for tripartite complex formation. The microcephaly-associated p80 S538L substitution also blocked the binding of ASPMp (Fig. 4e), suggesting that the loss of ASPM association might partially underlie the microcephaly phenotype. Finally, mutation of the conserved phenylalanine residues in the first and fourth repeat of ASPM (F302A/F377A) strongly reduced the binding between full-length ASPM and katanin (Fig. 4f,g), demonstrating that tandem ASPM repeats cooperate in katanin binding. Taken together, these results demonstrate that formation of the ASPM–katanin complex depends on residues located at the interface of the p60/p80 heterodimer and on conserved residues in the linear motifs of ASPM.

ASPM associates with microtubule minus ends *in vitro* and in cells

To understand how ASPM and katanin work together, we set out to reconstitute their activities *in vitro*. To this end, we purified the short isoform of mouse ASPM in complex with calmodulin from overexpressing HEK293T cells (GFP-ASPM; Fig. 3a and Supplementary Fig. 7a). ASPM decorated GMPCPP-stabilized microtubules in the absence of free tubulin; however, when tubulin was added even at a concentration insufficient to induce polymerization, ASPM preferentially localized to microtubule minus ends, as determined by co-localization with the microtubule minus-end marker CAMSAP3 (ref. 34) (Fig. 5a,b). At tubulin concentrations supporting microtubule polymerization, ASPM strongly accumulated at growing microtubule minus ends and slowed down their growth. This effect was more pronounced at higher ASPM concentrations, when both the enrichment of ASPM and its binding frequency at the minus ends were higher (Fig. 5c–h). At ASPM concentrations above 20 nM, a complete block of minus-end outgrowth was observed (Fig. 5d–f); at such higher concentrations, ASPM also regained microtubule lattice binding (Fig. 5d,e,g).

To assess which parts of ASPM confer microtubule minus-end-binding specificity, we performed deletion mapping of the mouse protein and found that its minus-end binding does not require the C-terminal HEAT and IQ repeats (Fig. 5i,j and Supplementary Fig. 7a); shorter fragments could not be assayed due to their propensity to aggregate. Fly Asp and worm ASPM-1 also accumulated at growing microtubule minus ends *in vitro* (Fig. 5k,l and Supplementary Fig. 7a), and we found that the first three conserved CH domains (CH1-CH3) of worm ASPM-1 were sufficient for this activity (Fig. 5m and Supplementary Fig. 7a). Mass spectrometry analysis of different ASPM preparations revealed no other microtubule-associated proteins (MAPs, Supplementary Table 4), supporting the conclusion that minus-end tracking is an autonomous activity of ASPM.

The specific minus-end binding of worm ASPM-1 and its CH1-CH3 fragment was confirmed in interphase mammalian cells (Fig. 5n,o and Supplementary Fig. 4a,b). Mouse ASPM could not be analysed in a similar way because it strongly accumulated in the nucleus during interphase. However, spindle microtubule

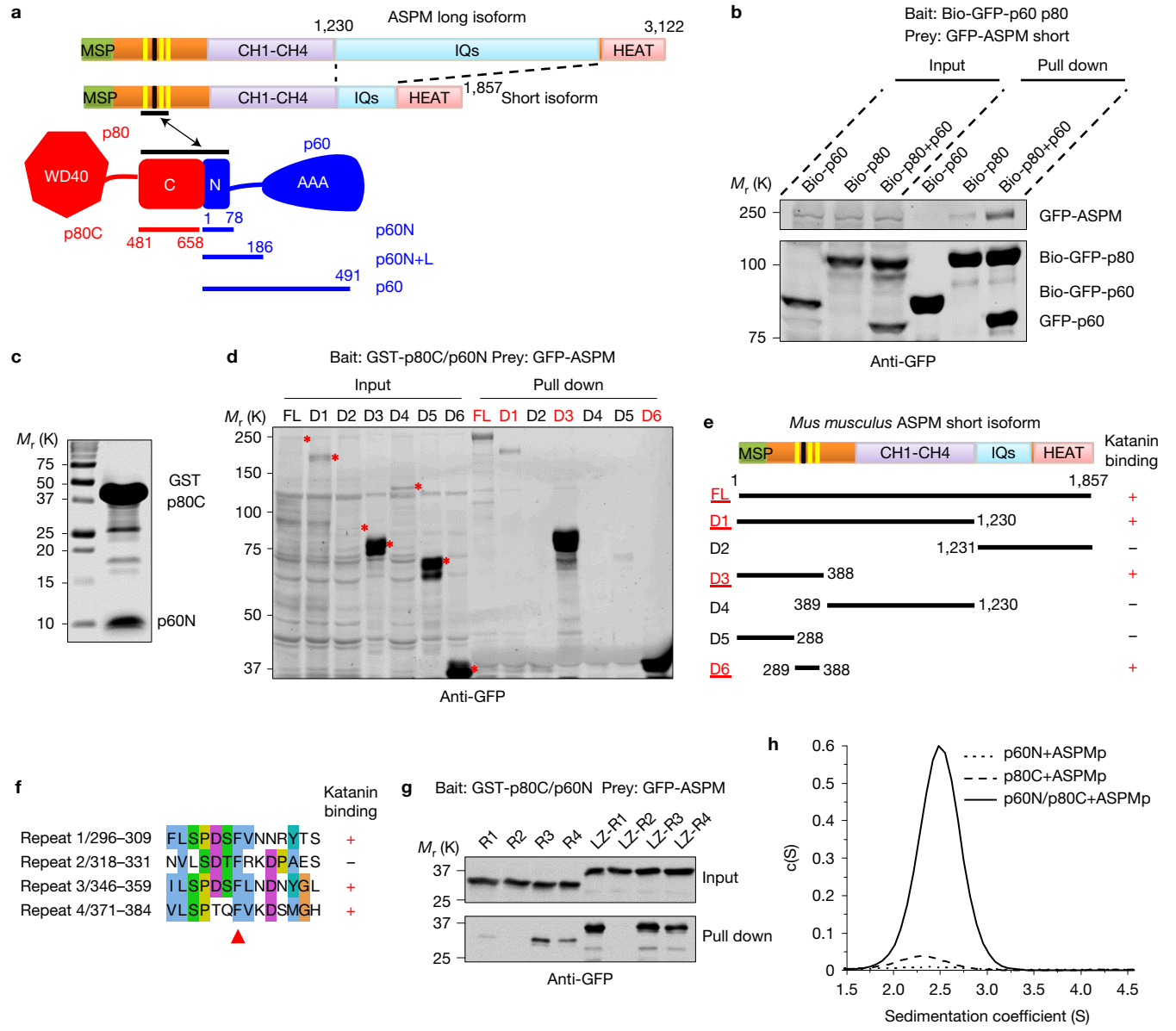

Figure 3 The interaction between ASPM and katanin requires a conserved repeat sequence of ASPM and the p60N/p80C heterodimer. (**a**) Scheme of the domain organization of ASPM, p60 and p80. Three (yellow) out of four linear repeats in ASPM interact with p60N/p80C. The numbering is based on the mouse protein. (**b**) Streptavidin pull down assay with lysates of HEK293T cells expressing individual subunits of katanin or the p60/p80 heterodimer together with the short isoform of ASPM. A substrate peptide for the biotin ligase BirA (Bio-tag, MASGLNDIFEAQKIEWHE) was inserted at the N terminus of GFP-tagged bait proteins. Biotinylation was accomplished by co-expressing the tagged proteins together with BirA. (**c**) Coomassie blue staining of a gel with GST-p80C/p60N purified from *E. coli*, which was used for the GST pull down assays in **d** and **g** and Fig. 4f,g. (**d**,**e**) western blotting and a summary of the mapping of the interaction between ASPM and p60N/p80C: lysates of HEK293T cells expressing full-length ASPM or fragments thereof were used for GST pull down assays with GST-p80C/p60N. (**f**) Alignment of the four repeats present in the mouse ASPM protein. Red arrowhead, a conserved phenylalanine residue, corresponding to F352 in the third repeat. (**g**) GST-p80C/p60N pull down assay with lysates of HEK293T cells expressing different GFP-tagged ASPM peptide repeats in monomeric or dimeric forms. LZ, leucine zipper from GCN4, which was used as a dimerization domain. The p60N/p80C heterodimer did not bind to the second repeat of ASPM and preferentially associated with the third repeat when the repeats were tested as monomers. (**h**) Continuous sedimentation coefficient distribution profiles c(S) showing that p60N/p80C complex formation is a prerequisite for ASPMp peptide binding. TAMRA-labelled ASPMp peptide was detected at 555 nm. When mixed with either p60N or p80C alone, the unbound ASPMp peptide, because of its small size, did not produce any signal between 1.5 and 4.5 S. In contrast, upon the addition of the ASPMp peptide to the p60N/p80C complex, a peak at 2.5 S appeared, demonstrating binding of the peptide to the complex. Unprocessed original scans of blots are shown in Supplementary Fig. 8.

photoablation experiments showed that besides weak lattice binding, the endogenous GFP-tagged ASPM localized to freshly generated minus ends within 7.0 ± 2.4 s after ablation, and moved to the spindle pole with a speed of 3.1 ± 1.4 μm min^{-1} (mean ± s.d., $n = 13$, Fig. 5p). This dynamic behaviour is similar to that of the NuMA–dynein complex after photoablation of spindle microtubules[28,29]. We

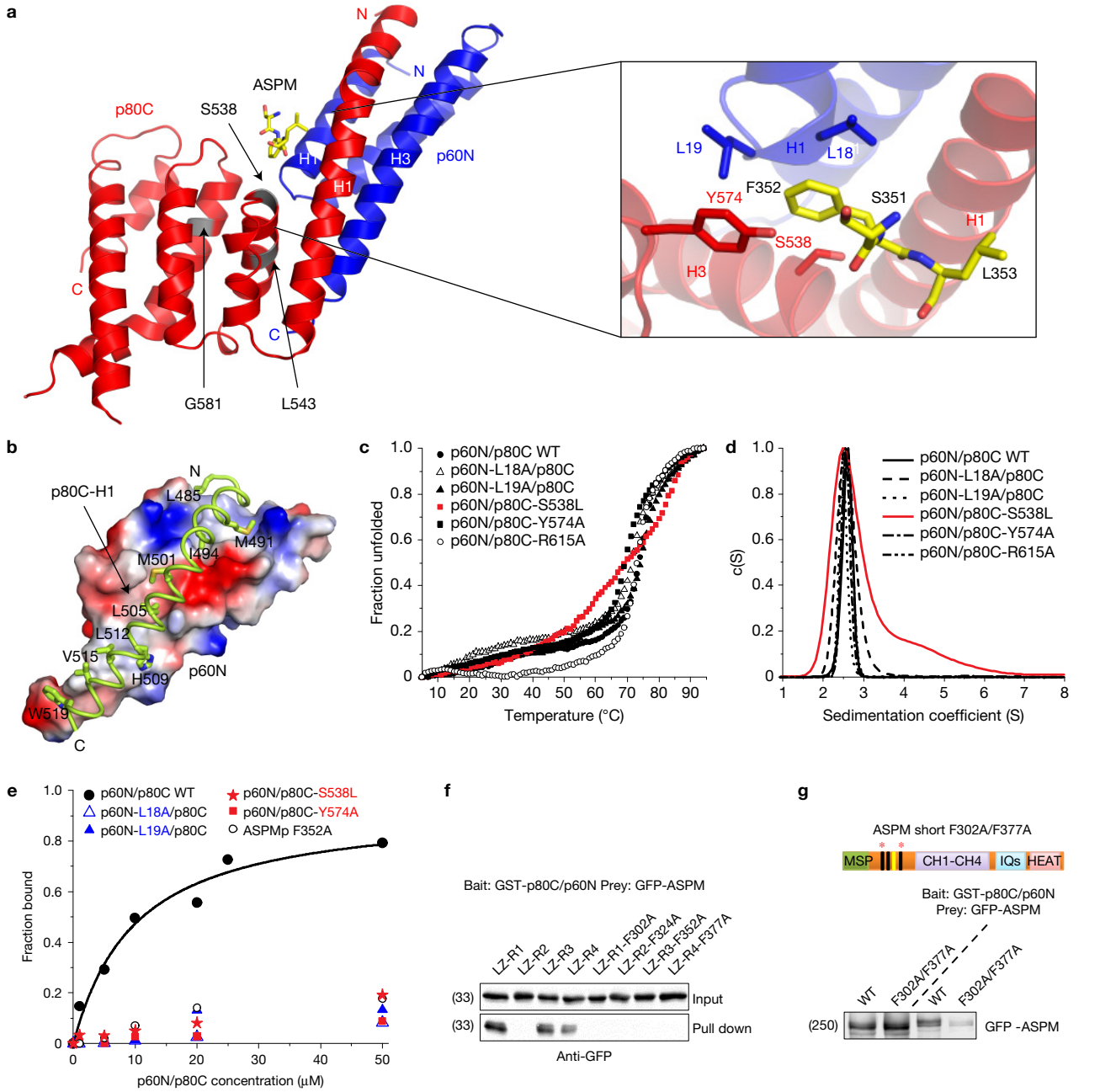

Figure 4 Structure of the p60N/p80C/ASPMp complex. (**a**) Ribbon representation of the p60N/p80C/ASPMp complex structure and close-up view of the ASPMp-binding site with interacting residues shown in stick representation. The position of the three microcephaly-associated mutations in the p80C subunit—S538L, L543R and G581D—are highlighted in grey. (**b**) Close-up view of the hydrophobic interactions between p60N (shown as electrostatic surface representation; positively-, negatively- and hydrophobic residues are depicted in blue, red and grey, respectively) and helix H1 of p80C (shown as a ribbon representation with hydrophobic residues in stick representation). (**c**) Normalized thermal unfolding profiles of p60N/p80C complex variants assessed by circular dichroism spectroscopy. All mutants display stabilities comparable to the wild-type protein except for the S538L mutant (red), which is 6 °C less stable. We could not purify the L543R and G581D mutants from *E. coli*, most likely because these mutations affect the fold and/or stability of the p60N/p80C complex. (**d**) Continuous sedimentation coefficient distribution profiles c(S) of p60N/p80C showing that mutations p60N-L18A, p60N-L19A, p80C-Y574A and p80C-R615A did not affect p60N/p80C heterodimer formation. The microcephaly-associated mutation S538L (red) did show signs of aggregation. (**e**) Binding curves obtained from sedimentation velocity experiments for the interaction between the TAMRA-labelled ASPM peptide and p60N/p80C. The ASPM peptide interacts with p60N/p80C with an apparent dissociation constant, K_d, of 9 μM. The individual substitutions F352A of ASPM, L18A or L19A of p60N, or S538L or Y574A of p80C abolished the interactions between the TAMRA-ASPM peptide and p60N/p80C. (**f**) GST-p80C/p60N pull down assays with lysates of HEK293T cells expressing either the WT ASPM peptide repeats or their mutated versions, in which the conserved phenylalanine residue (red arrowhead in Fig. 3f), was substituted for alanine (FA). (**g**) GST-p80C/p60N pull down assays with lysates of HEK293T cells expressing either the WT full-length ASPM or the F302A/F377A mutant, in which the conserved phenylalanine residues of repeats 1 and 4 of ASPM have been simultaneously mutated to alanines. Unprocessed original scans of blots are shown in Supplementary Fig. 8.

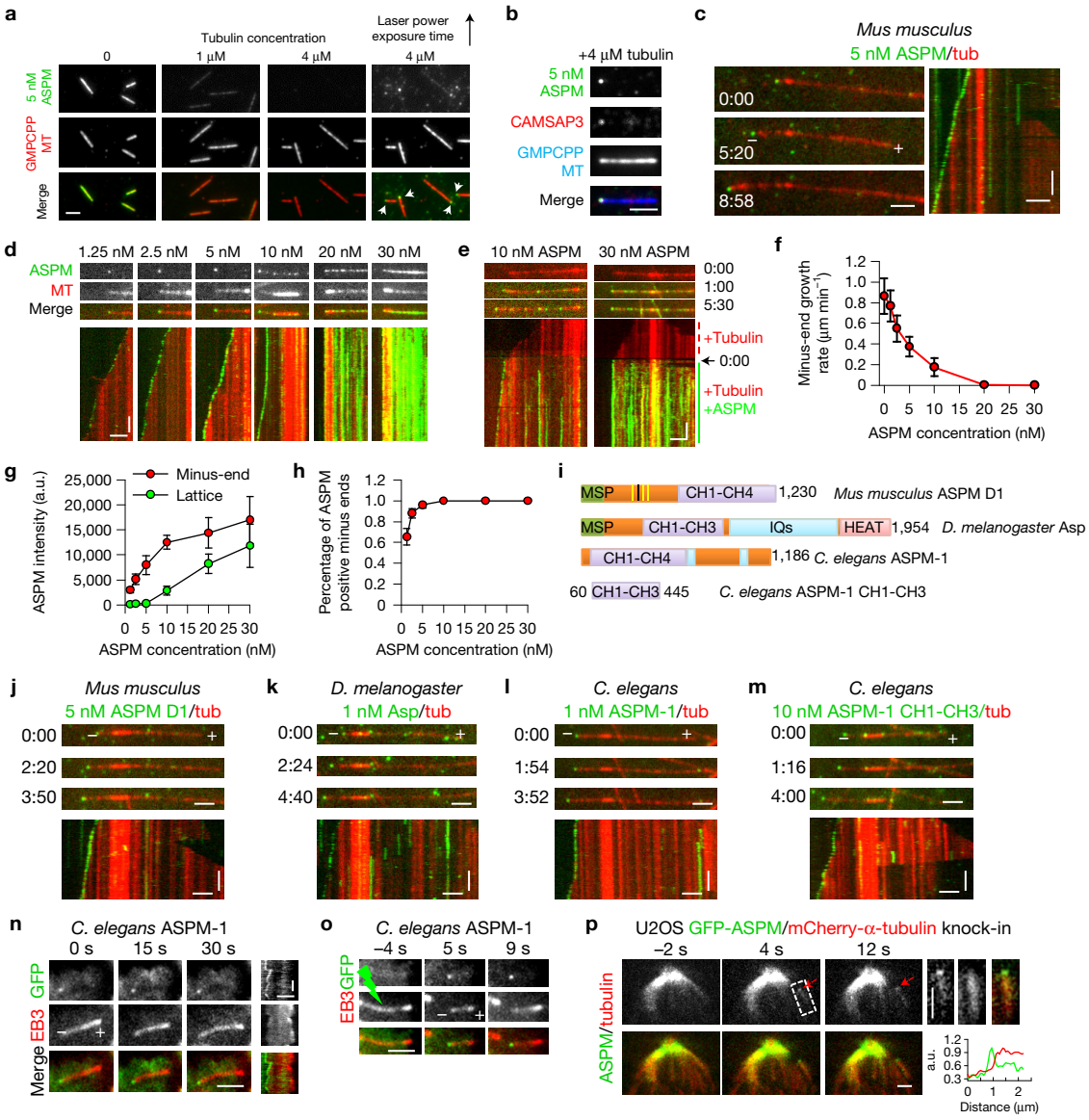

Figure 5 ASPM associates with microtubule minus ends *in vitro* and in cells. (**a**) Images of mouse GFP-ASPM (green) binding to stable GMPCPP-stabilized microtubules (red) in the presence of tubulin at different concentrations. White arrowheads indicate ASPM specifically associated with one microtubule end. Scale bar, 2 μm. (**b**) Images showing co-localization of GFP-ASPM (green) and SNAP-Alexa647-CAMSAP3 (red) at the minus end of a GMPCPP-stabilized microtubule (blue). Scale bar, 2 μm. (**c**,**d**,**j**–**m**) Images and corresponding kymographs of GFP-full-length ASPM (**c**,**d**), ASPM D1 (**j**), fly Asp (**k**), worm ASPM-1 full-length (**l**) and CH1-CH3 (**m**) (green) tracking dynamic microtubule minus ends (red). Scale bars: horizontal, 2 μm; vertical, 1 min. (**e**) Images and corresponding kymographs of GFP-tagged full-length ASPM tracking (10 nM) or blocking (30 nM) dynamic microtubule minus ends (red) in a flow-in experiment. 0:00, the moment of flow-in. Scale bars: horizontal, 2 μm; vertical, 1 min. (**f**) Quantification of minus-end growth rate in the presence of ASPM at different concentrations. $n = 49$, 41, 37, 29, 28, 30 and 30 microtubules for ASPM concentration from 0 to 30 nM, (**g**,**h**) ASPM intensity on microtubule minus ends and lattice, and percentage of ASPM-positive minus ends; At ASPM concentration from 1.25 to 30 nM, $n = 22$, 12, 11, 12, 13 and 13 microtubules (end intensity and accumulation frequency measurement); $n = 20$, 20, 19, 15, 19 and 20 microtubules (lattice intensity). Minus-end intensity of ASPM was averaged only over the time points at which ASPM accumulation was present. (**i**) A scheme of the domain organization of mouse ASPM D1, fly Asp and worm ASPM-1. (**n**,**o**) Full-length worm ASPM-1 associates with minus ends of free microtubules (**n**) or minus ends freshly generated by photoablation (**o**) in interphase MRC5 cells. Green lightning bolt indicates the site of photoablation. Scale bars, horizontal, 2 μm; vertical, 10 s. (**p**) Images of a GFP-ASPM and mCherry-α-tubulin double knock-in cell before and after photoablation. Enlarged images at 4 s and the corresponding line scan of the two channels are shown on the right. Scale bars, 2 μm. Time represented as min:s. Data represent mean ± s.d. Source data for **f**–**h** can be found in Supplementary Table 5.

conclude that ASPM can autonomously localize to microtubule minus ends and that this activity is evolutionarily conserved. Furthermore, at high concentrations ASPM can completely block minus-end growth and associate with microtubule lattice.

The katanin p60/p80 heterodimer binds and bends microtubule ends in cells and *in vitro*

Next, we investigated whether katanin can also interact with microtubule ends. In cells, overexpressed p60/p80 frequently localized

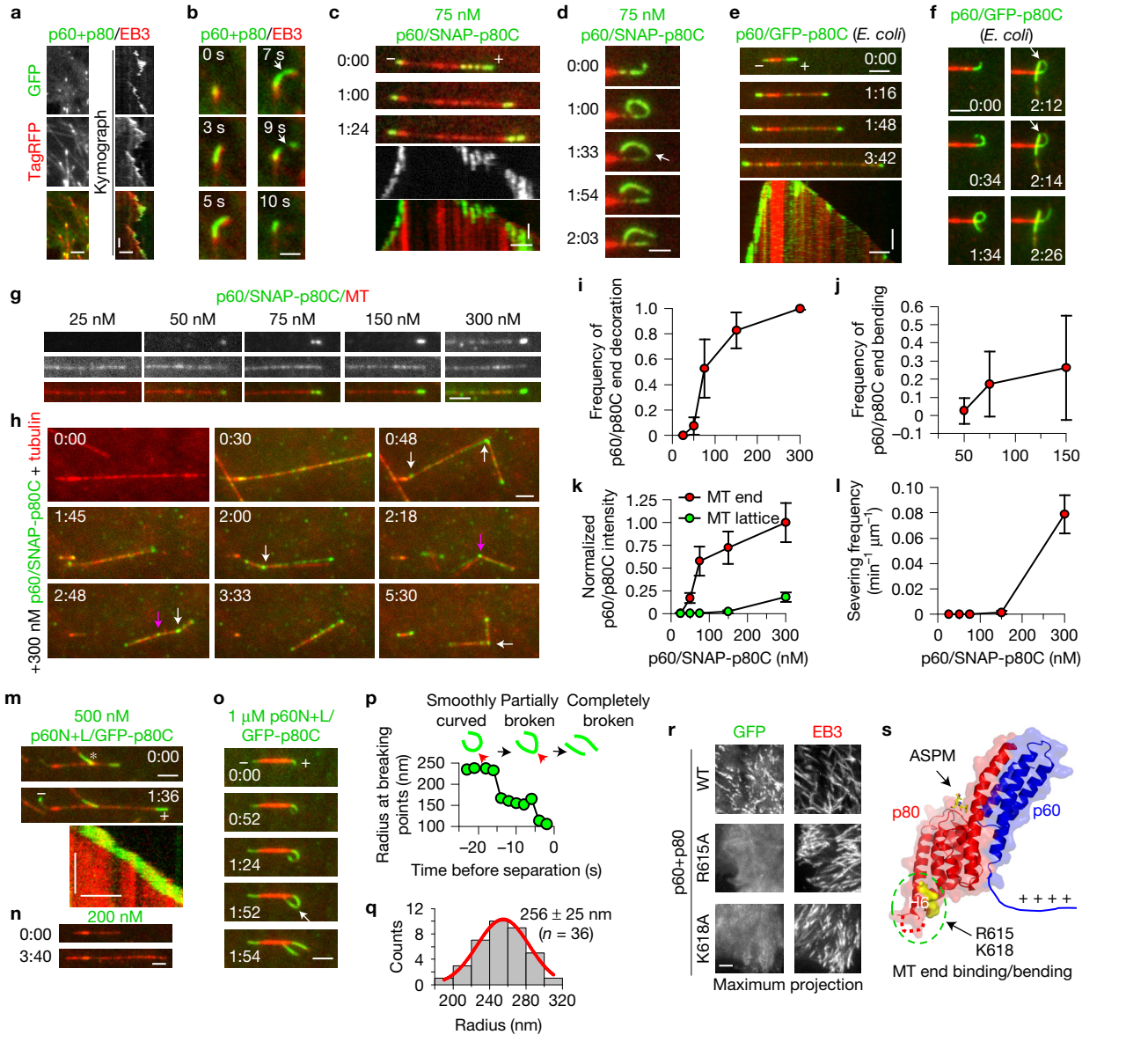

Figure 6 The katanin p60/p80 complex binds and bends microtubule ends in cells and *in vitro*. (**a**) Images and kymographs of the co-localization of GFP-p60/p80 and EB3-TagRFP in MRC5 cells. Scale bars: horizontal, 2 µm; vertical, 10 s. (**b**) Images of a single microtubule plus end bound to GFP-p60/p80 and EB3-TagRFP. White arrow, breaking of a bent microtubule end. Scale bar, 1 µm. (**c**–**f**,**m**–**o**) Images and corresponding kymographs illustrating the behaviour of p60/SNAP-Alexa647-p80C (**c**,**d**), p60/GFP-p80C (**e**,**f**, purified from *E. coli*) and p60N+L/GFP-p80C (**m**–**o**) on dynamic microtubule ends *in vitro*; white arrow, breaking of a bent microtubule. Scale bars, horizontal, 2 µm; vertical, 1 min. White asterisk in **m** denotes the signal from another microtubule. (**g**) Images of p60/SNAP-Alexa647-p80C localizing to dynamic microtubule plus ends and lattices at different concentrations. Scale bar, 2 µm. (**h**) Images of p60/SNAP-Alexa647-p80C severing dynamic microtubules at 300 nM in a flow-in experiment. White and purple arrows indicate complete and incomplete severing events, respectively. The misalignment between different channels was the result of sequential imaging of freely moving microtubules. Scale bar, 2 µm. (**i**,**j**) Frequency of p60/p80C accumulation and bending of growing plus ends at different concentrations. At 300 nM, end bending could not be reliably measured due to movement of severed microtubules. **i**, $n = 22$, 23, 24, 20 and 19 microtubules (25–300 nM); **j**, $n = 23$, 24 and 21 microtubules (50–150 nM). (**k**) Intensities of p60/p80C on microtubule ends and lattices at different concentrations. $n = 100$, 101, 110, 100 and 100 microtubules (25–300 nM). (**l**) Severing activity of p60/p80C on dynamic microtubules at different concentrations. $n = 2$ (25–75 nM) or 3 (150–300 nM) experiments. (**p**) Quantification of the radius of p60N+L/p80C decorated microtubule during a bending and breaking event. (**q**) Histogram of radii of microtubule curvature induced by p60N+L/p80C; $n = 36$ microtubules. (**r**) Maximum projection of 100 s time lapse movies of indicated GFP-p60/p80 variants co-expressed with EB3-TagRFP in HeLa cells. Scale bar, 2 µm. (**s**) Structural illustration of the positions of key residues of p60N/p80C required for microtubule end decoration. Time in min:s. Data represent mean ± s.d. Source data for **i**–**l**,**q** can be found in Supplementary Table 5.

to growing microtubule tips labelled with the plus-end marker EB3 and caused their bending and breakage (Fig. 6a,b and Supplementary Video 2). This microtubule end localization required simultaneous expression of the p60 subunit and the p80 C terminus, but was independent of the WD40 domain of p80 (Supplementary Fig. 5a–c). *In vitro*, the p60/p80C complex purified from HEK293T cells

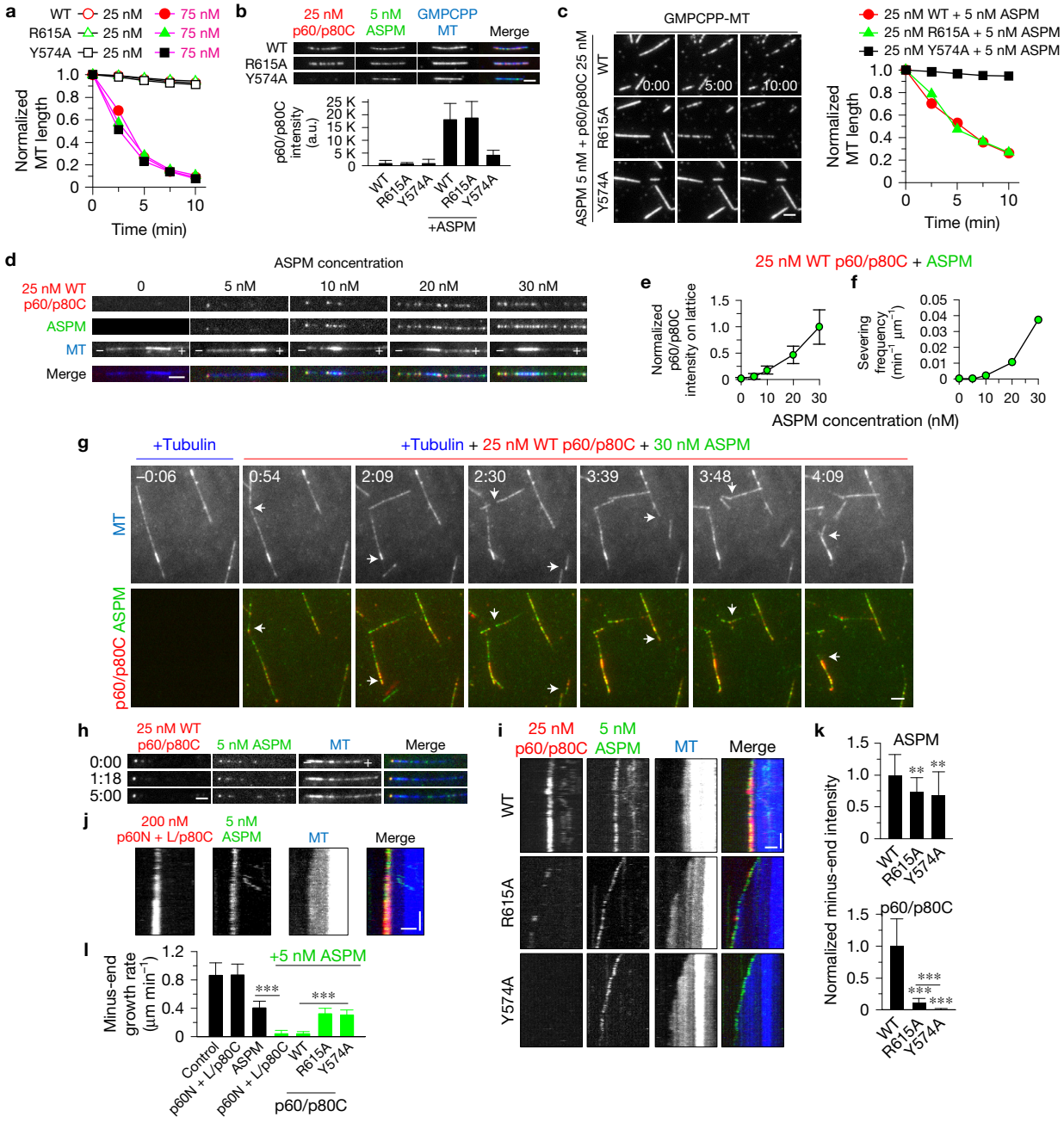

Figure 7 The ASPM–katanin complex severs microtubules and blocks minus-end growth *in vitro*. (**a**) Quantification of microtubule-severing activity of 25 nM (black lines) and 75 nM (purple lines) p60/SNAP-Alexa647-p80C (wild type (WT) and mutants). For microtubule images, see Supplementary Fig. 6c. Data are the mean of 2 experiments. (**b**) Images and quantification of the recruitment of 25 nM p60/SNAP-Alexa647-p80C (red) to GMPCPP-stabilized microtubules (blue) in the presence of 5 nM GFP-ASPM (green). From left to right, $n=47$, 47, 49, 49, 45 and 52 microtubules. (**c**) Images and quantification of microtubule-severing activity of 25 nM p60/SNAP-Alexa647-p80C (WT and mutants) in the presence of 5 nM GFP-ASPM. Data are the mean of 2 experiments. (**d**) Images showing recruitment of WT p60/SNAP-Alexa647-p80C onto dynamic microtubule minus ends and lattices by GFP-ASPM at different concentrations. (**e**) Quantification of microtubule lattice intensity of WT p60/SNAP-Alexa647-p80C at different ASPM concentrations. From left to right, $n=65$, 63, 71, 65 and 64 microtubules. (**f**) Quantification of severing activity of WT p60/SNAP-Alexa647-p80C at different ASPM concentrations. Data are the mean of 2 experiments. (**g**) TIRFM time lapse images of severing of dynamic microtubules by 25 nM WT p60/SNAP-Alexa647-p80C and 30 nM GFP-ASPM. White arrows indicate severing events. (**h**) Images showing recruitment of WT p60/SNAP-Alexa647-p80C to dynamic microtubule minus ends by 5 M GFP-ASPM. (**i**,**j**) Kymographs showing localization of GFP-ASPM and WT p60/SNAP-Alexa647-p80C, R615A and Y574A mutants (**i**) or p60N+L/SNAP-Alexa647-p80C (**j**) to dynamic microtubule minus ends. Vertical scale bar, 1 min. (**k**) Quantification of ASPM and p60/SNAP-Alexa647-p80C intensities on minus ends. From left to right, ASPM, $n=32$, 19 and 19 microtubules; p60/p80C, $n=33$, 19 and 19 microtubules. (**l**) Quantification of minus-end growth rate in conditions with 200 nM p60N+L/p80C alone, 5 nM ASPM alone, and 5 nM ASPM together with 200 nM p60N+L/p80C or 25 nM p60/p80C (WT, R615A and Y574A). From left to right, $n=49$, 41, 38, 55, 58, 96, 84 microtubules. The data for control were re-plotted from Fig. 5f. Horizontal scale bars in all panels, 2 µm. Data represent mean ± s.d. $^{**}P<0.01$; $^{***}P<0.001$, Mann–Whitney *U* test. Time in min:s. Source data for **a**–**c**,**e**,**f**,**k**,**l** can be found in Supplementary Table 5.

(Supplementary Fig. 7b) readily severed stabilized microtubules at 75 nM (see below); but, similar to p60 alone *in vitro*[26], this activity was strongly inhibited in the presence of free tubulin. However, and in agreement with cellular data, 75 nM purified p60/p80C heterodimer could track, decorate, bend and break growing microtubule plus and minus ends (Fig. 6c,d; see Fig. 6i,j for end binding and bending frequency). These activities were not mediated by additional factors that were co-purified from HEK293T cells, as we detected no other MAPs in our purifications (Supplementary Table 4). Furthermore, the p60/p80C complex purified from *E. coli* (Supplementary Fig. 7b) also showed robust microtubule end-binding, end-bending and end-breaking activities (Fig. 6e,f).

To get further insight into the end-binding and severing activities of katanin, different concentrations of p60/p80C together with 20 μM tubulin were flowed into the reaction chamber containing pre-assembled dynamic microtubules (Fig. 6g–h and Supplementary Fig. 5d). The intensity of katanin and its binding frequency to microtubule ends had a sigmoid-like response at 50–300 nM concentration (Fig. 6i,k), suggesting cooperative binding. In contrast, p60/p80C concentrations ≥300 nM were needed to observe katanin binding along pre-existing microtubules and microtubule severing (Fig. 6h,l, white arrows; Supplementary Video 3). Complete severing within one minute was observed at 750 nM p60/p80C (Supplementary Fig. 5d). Strikingly, no microtubule severing was observed in the vicinity of the ends, although the p60/p80C intensity was much higher near the ends than along microtubules. This result suggests that the end-decorating pool of katanin is much less potent, if not incapable, of microtubule severing compared to its lattice pool.

While the p60N/p80C heterodimer did not bind to microtubule ends, the p60N+L/p80C complex (Supplementary Fig. 7b), which includes the positively charged linker (L) adjacent to p60N but lacks the ATPase domain, displayed robust microtubule end-tracking, -bending and -breaking activity when present at concentrations of ≥0.5 μM (Fig. 6m–o and Supplementary Video 4). The ATPase domain of p60 is thus not essential for microtubule end decoration and breaking, but probably contributes to this activity by directly interacting with microtubules or by promoting katanin oligomerization. The radius of p60N+L/p80C decorated and bent microtubule ends before breakage was 256 ± 25 nm (mean ± s.d., $n = 36$; Fig. 6p,q), which corresponds to a 1.8°± 0.2° angle between two longitudinally arranged tubulin dimers. This degree of curvature is significantly smaller than that of free tubulin or tubulin in complex with stathmin[35], but similar to the curvature of tubulin sheets at growing microtubule ends[36], suggesting a plausible growing end recognition mechanism.

Based on the crystal structure of the p60N/p80C/ASPMp complex, we identified positively charged surface-exposed residue patches on p60N/p80C, which might bind to the negatively charged microtubule lattice. Mutation analysis showed that two highly conserved residues, R615 and K618 in helix H6 of p80C, but not any of the other arginine or lysine residues used as controls were essential for microtubule end binding in cells (Fig. 6r,s and Supplementary Fig. 5e–g). The highly conserved four-residue segment 607–610 located in the loop connecting helices H5 and H6 was also required for the interaction with microtubule ends (Supplementary Fig. 5f,g). The N-terminal part of p60 and the C-terminal part of p80 thus form a microtubule-binding module that recognizes and bends microtubule ends through a combination of a conserved positively charged surface patch at the tip of p80 and a positively charged linker present in the p60 subunit (Fig. 6s).

The ASPM–katanin complex severs microtubules and blocks minus-end growth *in vitro*

Having established that both ASPM and the p60/p80C heterodimer specifically interact with microtubule ends at low concentration and associate with microtubule lattice at high concentration, we next tested their combined activities using either wild-type p60/p80C or the two p80C mutants, R615A and Y574A, which are deficient in binding to dynamic microtubule ends or ASPM, respectively (Supplementary Fig. 6a,b and Fig. 4e). In the absence of free tubulin, all three p60/p80C variants could efficiently sever microtubules when present at concentrations of ≥75 nM, but not at 25 nM (Fig. 7a and Supplementary Fig. 6c). Upon the addition of 5 nM ASPM, both the wild-type and the R615A p60/p80C variants, but not the ASPM binding-deficient Y574A mutant, displayed strong microtubule recruitment and severing at 25 nM concentration (Fig. 7b,c). ASPM can thus enhance the activity of katanin by recruiting it to microtubules. Under these conditions, the R615A mutant could sever microtubules as robustly as wild-type p60/p80C, again suggesting that the microtubule end-binding and severing activities of katanin are biochemically distinct.

We then asked whether ASPM can promote microtubule severing by katanin in the presence of free tubulin, and found that while 25 nM p60/p80C alone did not bind or sever dynamic microtubules, increasing concentrations of ASPM caused its recruitment to microtubules and their severing (Fig. 7d–g and Supplementary Video 5). Upon the addition of 30 nM ASPM, 25 nM p60/p80C displayed a severing activity that was approximately half of that observed with 300 nM p60/p80C alone (Figs 6l and 7f), which is close to an order of magnitude of improvement. The R615A but not the Y574A mutant of p60/p80C was able to sever dynamic microtubules at 25 nM concentration in the presence of 30 nM wild-type ASPM (Supplementary Fig. 6d–g), while no increase in severing was observed with 30 nM ASPM F302A/F377A, which is deficient in katanin binding (Supplementary Fig. 6h–j). These data demonstrate that katanin-mediated microtubule severing is promoted by the direct interaction with ASPM but does not require katanin's microtubule end-binding activity.

Next, we investigated whether katanin can enhance the minus-end blocking by ASPM. 5 nM wild-type ASPM, but not the F302A/F377A mutant that is deficient in katanin binding, was sufficient to recruit 25 nM p60/p80C onto microtubule minus ends (Fig. 7d and Supplementary Fig. 6k–m), and this coincided with a dramatic suppression of their growth (Fig. 7h,i,k,l). In contrast, the R615A and the Y574A mutants showed only weak or no ASPM-mediated minus-end binding activity, respectively, and neither of the mutants could block minus-end elongation (Fig. 7i,k,l). The intensity of the ASPM signal at microtubule minus ends was higher in the presence of wild-type p60/p80C than with the two mutant heterodimers (Fig. 7k), explaining the strong inhibition of minus-end growth. ASPM and katanin thus enhance each other's minus-end accumulation, in line with their mutual interdependence for spindle pole localization (Fig. 1d–f).

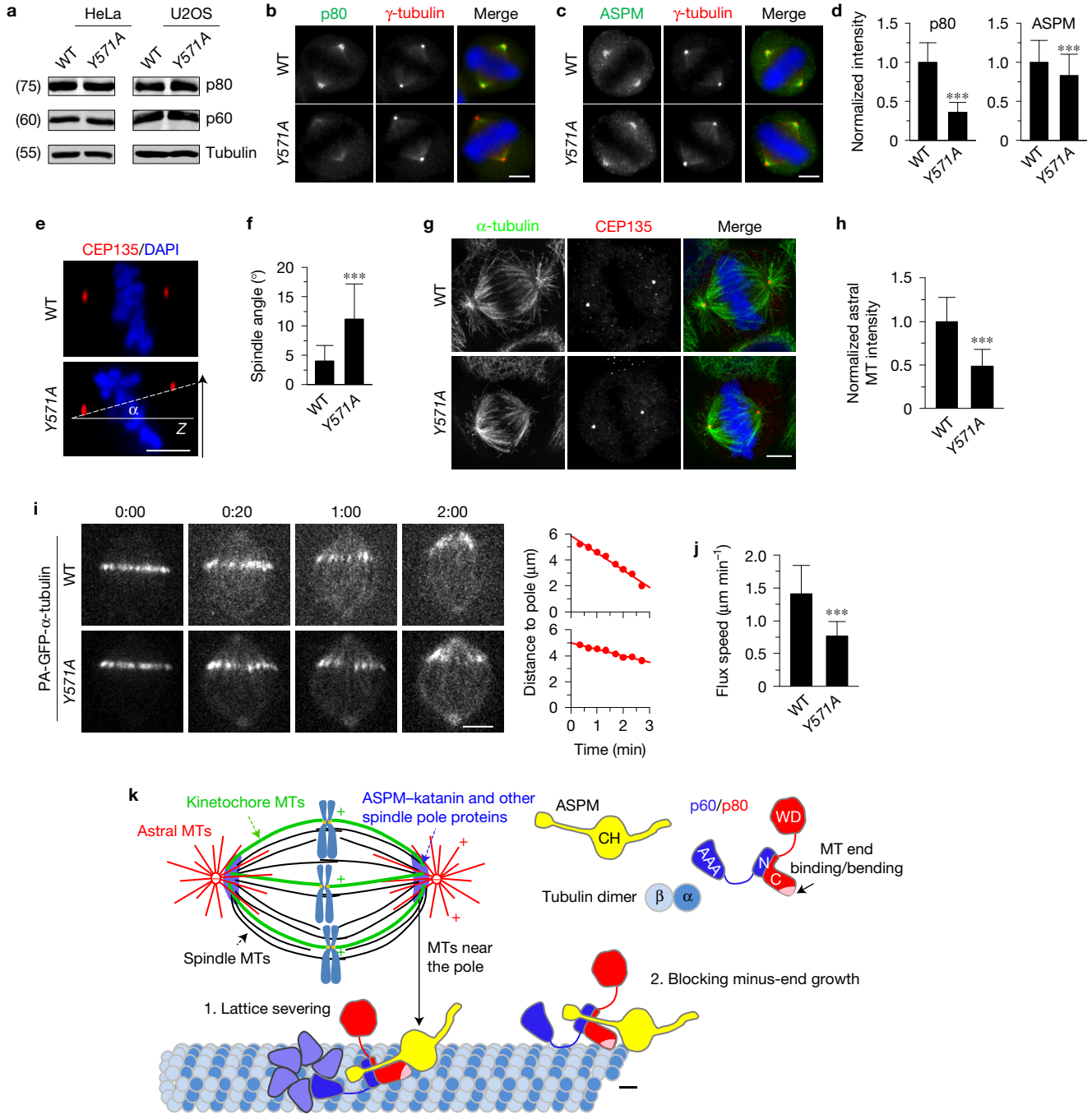

Figure 8 Dissociation of katanin from ASPM impairs spindle orientation and poleward flux. (**a**) western blotting with the indicated antibodies of extracts of wild-type (WT) and $p80^{Y571A}$ HeLa and U2OS cells. Katanin protein levels in WT and $p80^{Y571A}$ mutant cell lines are similar. (**b**–**d**) Immunofluorescence staining and quantification of p80 and ASPM intensities at spindle poles in WT and $p80^{Y571A}$ HeLa cells. For p80 intensity, $n=204$ spindle poles, WT; $n=220$, $p80^{Y571A}$; for ASPM intensity, $n=244$, WT; $n=240$, $p80^{Y571A}$. Scale bars, 5 μm. (**e**,**f**) Orthogonal view (x–z) of metaphase HeLa cells stained for CEP135 and DAPI in WT, $p80^{Y571A}$ HeLa cells (**e**) and quantification of spindle angles (**f**; $n=40$ cells, WT and $p80^{Y571A}$). Scale bar, 5 μm. (**g**) Immunostaining for α-tubulin, CEP135 and DNA (DAPI) in WT and $p80^{Y571A}$ HeLa cells. Maximum intensity projections of Z series with ~40 stacks and 200 nm step were shown here. Scale bar, 5 μm. (**h**) Quantification of astral microtubule intensity shown in **g**. $n=39$ (WT) and 41 ($p80^{Y571A}$) cells. Intensity was normalized to the average value in the WT cells. (**i**) Live cell images of spindle flux in WT and $p80^{Y571A}$ U2OS cells stably expressing PA-GFP-α-tubulin. Time displayed as min:s. Plots of the distance between photoactivated GFP stripe and the spindle pole over time are shown on the right. The flux speed was derived from the plot slopes. Scale bar, 5 μm. (**j**) Flux speed in WT and $p80^{Y571A}$ U2OS cells. $n=24$ (WT) and 28 ($p80^{Y571A}$) cells. (**k**) Model for regulation of microtubule minus-end dynamics at spindle poles by the ASPM–katanin complex. (1) Katanin recruited to microtubule lattice by ASPM can oligomerize through the p60 ATPase domain and sever microtubules. (2) Minus-end binding of the ASPM–katanin complex promotes its accumulation near the pole. Through its end-binding activity, katanin enhances blocking of microtubule minus-end growth by ASPM, which likely primes the minus ends for depolymerization by depolymerases. Data represent mean ± s.d. $^{***}P<0.001$, Mann–Whitney U test. Unprocessed original scans of blots are shown in Supplementary Fig. 8. Source data for **d**,**f**,**h**,**j** can be found in Supplementary Table 5.

Similarly, 200 nM p60N+L/p80C heterodimer could be recruited to microtubule minus ends by 5 nM ASPM and caused minus-end growth inhibition (Fig. 7j,l). However, by itself this truncated version of katanin, which lacks the ATPase domain, did not localize to microtubule ends at 200 nM (Fig. 6n). Taken together, these *in vitro* data indicate that ASPM and katanin mutually stimulate each other's activities: ASPM enhances the microtubule lattice severing activity of katanin; conversely, katanin promotes the ASPM-dependent blockage of microtubule minus-end growth.

Dissociation of katanin from ASPM impairs spindle orientation and poleward flux

Finally, to investigate the physiological role of the interaction between ASPM and katanin, we introduced in HeLa and U2OS cells a point mutation corresponding to the mouse p80 Y574A (Y571A in human) using CRISPR/Cas9 technology. The protein levels of p60 and p80 were comparable in wild-type and $p80^{Y571A}$ cells (Fig. 8a), which is consistent with our biophysical data showing that this mutation did not affect formation of a stable p60/p80 heterodimer (Fig. 4c,d). In line with the biochemical data and *in vitro* reconstitution assays, the intensity of spindle pole localization of katanin p80 Y571A was reduced to a level similar to that of the ASPM knockout (Fig. 8b,d). We also observed a decrease in ASPM intensity at the spindle pole in $p80^{Y571A}$ cells (Fig. 8c,d), confirming the mutual dependence of ASPM and katanin for pole localization. Furthermore, $p80^{Y571A}$ cells displayed defects in spindle orientation, astral microtubule density and poleward microtubule flux, similar to the ASPM knockout (Fig. 8e–j). Together, these data fully support our conclusion that the ASPM–katanin complex plays an important role in regulating microtubule dynamics at spindle poles.

DISCUSSION

The results of this study demonstrate that in mammalian cells, ASPM and katanin form a physiological complex that plays a key role in regulating spindle poles. They uncover the structural basis of the formation of the katanin p60/p80 heterodimer and its interaction with ASPM. The data further provide insight into selected mutations associated with microcephaly by showing that disease-relevant residue substitutions in the p80 subunit of katanin interfere with the activity of the protein by either destabilizing its fold or by disrupting the binding capacity of katanin for ASPM. Most importantly, our work reveals that the ASPM–katanin complex acts on both microtubule minus ends and the lattice, and shows that the combined activities of the two proteins can regulate microtubule dynamics at spindle poles.

We propose that ASPM and katanin can cooperate in two ways (Fig. 8k). First, due to its high local concentration at the poles resulting from preferential minus-end association, the ASPM–katanin complex could bind to and sever microtubules and thus directly contribute to microtubule disassembly at the poles. Second, ASPM can localize to the outmost microtubule minus ends and prevent their growth. The minus-end growth inhibiting activity of ASPM can be potentiated by the p60N+L/p80C module of katanin. Blocking minus-end growth in turn might make microtubules better substrates for depolymerases of the kinesin-13 family, which are involved in driving spindle flux by disassembling microtubule minus ends[32,37–39]. Along these lines, the kinesin-13 MCAK can efficiently accumulate at the ends of stable microtubules[40], but requires additional factors to bind and destabilize the ends of growing microtubules[41,42].

The demonstration that ASPM and katanin are microtubule end-binding proteins helps to understand their cellular activities. The function of fly Asp in centrosome-pole attachment, for example, might be explained by its dual affinity for microtubule minus ends and centrosomes[12], and worm ASPM-1 might rely on its ability to recognize microtubule minus ends to target the dynein–NuMA complex to spindle poles[7]. The R233Q mutation in the *C. elegans* p80 homologue, corresponding to our rationally introduced R615A mutation in mouse p80, has a synthetic interaction with the P99L mutant of the p60 homologue in controlling meiotic spindle length[24], supporting the *in vivo* significance of the end-binding and end-bending activity of katanin. These biochemical properties, which are distinct from microtubule severing, might also be the basis of katanin's role in regulating microtubule plus-end dynamics in interphase[34,43].

It has been hypothesized that during embryonic development, mitotic defects in neural precursors lead to microcephaly[44]. Here, we showed that ASPM and katanin knockout cells, as well as cells expressing a point mutant of katanin that cannot bind to ASPM, have defects in spindle orientation. It is possible that this abnormality is one of the factors contributing to perturbed cortical development. To conclude, our results connect two proteins known to be involved in microcephaly into the same biochemical pathway and suggest that proper regulation of microtubule minus ends during cell division is a critical factor for human brain development. □

METHODS

Methods, including statements of data availability and any associated accession codes and references, are available in the online version of this paper.

Note: Supplementary Information is available in the online version of the paper

ACKNOWLEDGEMENTS

We thank A. Prota for the help in refining the crystal structures, M. Boxem, C. Janke and M. Mikhaylova for the gift of materials, and the beamline scientists at beamlines X06DA of the Swiss Light Source (Paul Scherrer Institut, Villigen, Switzerland) for technical assistance with the X-ray data collection. This work was supported by the European Research Council Synergy grant 609822 and Netherlands Organization for Scientific Research (NWO) CW ECHO grant (711.011.005) to A.A., the EMBO long-term and Marie Curie IEF fellowships to L.R., grants from the Swiss National Science Foundation (31003A_166608 to M.O.S. and 31003A_163449 to R.A.K.), a NWO VIDI grant (723.012.102) to A.F.M.A. and as part of the National Roadmap Large-scale Research Facilities of the Netherlands (project number 184.032.201) to A.F.M.A. and A.J.R.H. The structural data reported in this paper are available in PDB (PDB code 5LB7).

AUTHOR CONTRIBUTIONS

K.J., L.R., S.H., R.A.K., M.O.S. and A.A. designed experiments, analysed data and wrote the paper. A.A. coordinated the project. K.J. and S.H. performed cellular and *in vitro* reconstitution experiments. L.R. performed biophysical experiments. L.R. and G.C. performed crystallography experiments. Q.L., A.F.M.A. and A.J.R.H. performed and analysed mass spectrometry experiments.

COMPETING FINANCIAL INTERESTS

The authors declare no competing financial interests.

Published online at http://dx.doi.org/10.1038/ncb3511

1. Morris-Rosendahl, D. J. & Kaindl, A. M. What next-generation sequencing (NGS) technology has enabled us to learn about primary autosomal recessive microcephaly (MCPH). *Mol. Cell Probes* **29,** 271–281 (2015).
2. Dammermann, A., Desai, A. & Oegema, K. The minus end in sight. *Curr. Biol.* **13,** R614–R624 (2003).
3. Rogers, G. C., Rogers, S. L. & Sharp, D. J. Spindle microtubules in flux. *J. Cell Sci.* **118,** 1105–1116 (2005).
4. Saunders, R. D., Avides, M. C., Howard, T., Gonzalez, C. & Glover, D. M. The *Drosophila* gene abnormal spindle encodes a novel microtubule-associated protein that associates with the polar regions of the mitotic spindle. *J. Cell Biol.* **137,** 881–890 (1997).
5. Wakefield, J. G., Bonaccorsi, S. & Gatti, M. The *Drosophila* protein asp is involved in microtubule organization during spindle formation and cytokinesis. *J. Cell Biol.* **153,** 637–648 (2001).
6. Fish, J. L., Kosodo, Y., Enard, W., Paabo, S. & Huttner, W. B. Aspm specifically maintains symmetric proliferative divisions of neuroepithelial cells. *Proc. Natl Acad. Sci. USA* **103,** 10438–10443 (2006).
7. van der Voet, M. *et al.* NuMA-related LIN-5, ASPM-1, calmodulin and dynein promote meiotic spindle rotation independently of cortical LIN-5/GPR/Gα. *Nat. Cell Biol.* **11,** 269–277 (2009).
8. Higgins, J. *et al.* Human ASPM participates in spindle organisation, spindle orientation and cytokinesis. *BMC Cell Biol.* **11,** 85 (2010).
9. Ito, A. & Goshima, G. Microcephaly protein Asp focuses the minus ends of spindle microtubules at the pole and within the spindle. *J. Cell Biol.* **211,** 999–1009 (2015).
10. Schoborg, T., Zajac, A. L., Fagerstrom, C. J., Guillen, R. X. & Rusan, N. M. An Asp–CaM complex is required for centrosome-pole cohesion and centrosome inheritance in neural stem cells. *J. Cell Biol.* **211,** 987–998 (2015).
11. Ripoll, P., Pimpinelli, S., Valdivia, M. M. & Avila, J. A cell division mutant of *Drosophila* with a functionally abnormal spindle. *Cell* **41,** 907–912 (1985).
12. do Carmo Avides, M. & Glover, D. M. Abnormal spindle protein, Asp, and the integrity of mitotic centrosomal microtubule organizing centers. *Science* **283,** 1733–1735 (1999).
13. Morales-Mulia, S. & Scholey, J. M. Spindle pole organization in *Drosophila* S2 cells by dynein, abnormal spindle protein (Asp), and KLP10A. *Mol. Biol. Cell* **16,** 3176–3186 (2005).
14. Bond, J. *et al.* ASPM is a major determinant of cerebral cortical size. *Nat. Genet.* **32,** 316–320 (2002).
15. Roll-Mecak, A. & McNally, F. J. Microtubule-severing enzymes. *Curr. Opin. Cell Biol.* **22,** 96–103 (2010).
16. McNally, F. J. & Vale, R. D. Identification of katanin, an ATPase that severs and disassembles stable microtubules. *Cell* **75,** 419–429 (1993).
17. Hartman, J. J. *et al.* Katanin, a microtubule-severing protein, is a novel AAA ATPase that targets to the centrosome using a WD40-containing subunit. *Cell* **93,** 277–287 (1998).
18. Mishra-Gorur, K. *et al.* Mutations in KATNB1 cause complex cerebral malformations by disrupting asymmetrically dividing neural progenitors. *Neuron* **84,** 1226–1239 (2014).
19. Hu, W. F. *et al.* Katanin p80 regulates human cortical development by limiting centriole and cilia number. *Neuron* **84,** 1240–1257 (2014).
20. McNally, K. P., Bazirgan, O. A. & McNally, F. J. Two domains of p80 katanin regulate microtubule severing and spindle pole targeting by p60 katanin. *J. Cell Sci.* **113,** 1623–1633 (2000).
21. Srayko, M., Buster, D. W., Bazirgan, O. A., McNally, F. J. & Mains, P. E. MEI-1/MEI-2 katanin-like microtubule severing activity is required for *Caenorhabditis elegans* meiosis. *Genes Dev.* **14,** 1072–1084 (2000).
22. McNally, K., Audhya, A., Oegema, K. & McNally, F. J. Katanin controls mitotic and meiotic spindle length. *J. Cell Biol.* **175,** 881–891 (2006).
23. McNally, K. P. & McNally, F. J. The spindle assembly function of *Caenorhabditis elegans* katanin does not require microtubule-severing activity. *Mol. Biol. Cell* **22,** 1550–1560 (2011).
24. McNally, K. *et al.* Katanin maintains meiotic metaphase chromosome alignment and spindle structure *in vivo* and has multiple effects on microtubules *in vitro*. *Mol. Biol. Cell* **25,** 1037–1049 (2014).
25. Loughlin, R., Wilbur, J. D., McNally, F. J., Nedelec, F. J. & Heald, R. Katanin contributes to interspecies spindle length scaling in Xenopus. *Cell* **147,** 1397–1407 (2011).
26. Bailey, M. E., Sackett, D. L. & Ross, J. L. Katanin severing and binding microtubules are inhibited by tubulin carboxy tails. *Biophys. J.* **109,** 2546–2561 (2015).
27. Cheung, K. *et al.* Proteomic analysis of the mammalian katanin family of microtubule-severing enzymes defines KATNBL1 as a regulator of mammalian katanin microtubule-severing. *Mol. Cell Proteomics* **15,** 1658–1669 (2016).
28. Elting, M. W., Hueschen, C. L., Udy, D. B. & Dumont, S. Force on spindle microtubule minus ends moves chromosomes. *J. Cell Biol.* **206,** 245–256 (2014).
29. Sikirzhytski, V. *et al.* Direct kinetochore-spindle pole connections are not required for chromosome segregation. *J. Cell Biol.* **206,** 231–243 (2014).
30. Gai, M. *et al.* ASPM and CITK regulate spindle orientation by affecting the dynamics of astral microtubules. *EMBO Rep.* **17,** 1396–1409 (2016).
31. Zhang, D., Rogers, G. C., Buster, D. W. & Sharp, D. J. Three microtubule severing enzymes contribute to the 'Pacman-flux' machinery that moves chromosomes. *J. Cell Biol.* **177,** 231–242 (2007).
32. Ganem, N. J., Upton, K. & Compton, D. A. Efficient mitosis in human cells lacking poleward microtubule flux. *Curr. Biol.* **15,** 1827–1832 (2005).
33. Iwaya, N. *et al.* A common substrate recognition mode conserved between katanin p60 and VPS4 governs microtubule severing and membrane skeleton reorganization. *J. Biol. Chem.* **285,** 16822–16829 (2010).
34. Jiang, K. *et al.* Microtubule minus-end stabilization by polymerization-driven CAMSAP deposition. *Dev. Cell* **28,** 295–309 (2014).
35. Brouhard, G. J. & Rice, L. M. The contribution of $\alpha\beta$-tubulin curvature to microtubule dynamics. *J. Cell Biol.* **207,** 323–334 (2014).
36. Janosi, I. M., Chretien, D. & Flyvbjerg, H. Modeling elastic properties of microtubule tips and walls. *Eur. Biophys. J.* **27,** 501–513 (1998).
37. Wang, H., Brust-Mascher, I., Civelekoglu-Scholey, G. & Scholey, J. M. Patronin mediates a switch from kinesin-13-dependent poleward flux to anaphase B spindle elongation. *J. Cell Biol.* **203,** 35–46 (2013).
38. Rogers, G. C. *et al.* Two mitotic kinesins cooperate to drive sister chromatid separation during anaphase. *Nature* **427,** 364–370 (2004).
39. Gaetz, J. & Kapoor, T. M. Dynein/dynactin regulate metaphase spindle length by targeting depolymerizing activities to spindle poles. *J. Cell Biol.* **166,** 465–471 (2004).
40. Desai, A., Verma, S., Mitchison, T. J. & Walczak, C. E. Kin I kinesins are microtubule-destabilizing enzymes. *Cell* **96,** 69–78 (1999).
41. Montenegro Gouveia, S. *et al. In vitro* reconstitution of the functional interplay between MCAK and EB3 at microtubule plus ends. *Curr. Biol.* **20,** 1717–1722 (2010).
42. Tanenbaum, M. E. *et al.* A complex of Kif18b and MCAK promotes microtubule depolymerization and is negatively regulated by Aurora kinases. *Curr. Biol.* **21,** 1356–1365 (2011).
43. Zhang, D. *et al. Drosophila* katanin is a microtubule depolymerase that regulates cortical-microtubule plus-end interactions and cell migration. *Nat. Cell Biol.* **13,** 361–370 (2011).
44. Taverna, E., Gotz, M. & Huttner, W. B. The cell biology of neurogenesis: toward an understanding of the development and evolution of the neocortex. *Annu. Rev. Cell Dev. Biol.* **30,** 465–502 (2014).

METHODS

Cell culture and transfection. Cell lines were cultured in DMEM/F10 (1:1) supplemented with 10% FBS and 5 U ml^{-1} penicillin and 50 µg ml^{-1} streptomycin. FuGENE6 (Promega) was used to transfect plasmids for immunofluorescence and live cell imaging; polyethylenimine (PEI, Polysciences) was used to transfect HEK293T cells for StrepTactin protein purification and GST, streptavidin pull down experiments. HEK293T, HeLa, U2OS and MRC5 cell lines used here were not found in the database of commonly misidentified cell lines maintained by ICLAC and NCBI BioSample, were not authenticated and were negative for mycoplasma contamination.

Antibodies. We used rabbit polyclonal antibodies against ASPM (Novus, NB100-2278, IF-1:100, WB-1:1,000), katanin p60 and p80 (Proteintech, 17560-1-AP and 14969-1-AP, IF-1:200, WB-1:1,000), GFP (Abcam, ab290, WB-1:2,500), CEP135 (Sigma-Aldrich, SAB4503685, IF-1:600), NuMA (Thermo Fisher, PA3-16829, IF-1:1,000), γ-tubulin (Sigma-Aldrich, T3559, IF-1:600), mouse monoclonal antibodies against β-tubulin (Sigma-Aldrich, T5201, WB-1:4,000), γ-tubulin (Sigma-Aldrich, T6557,IF-1:600), p150^{Glued} (BD Biosciences, 610474, IF-1:100), and a rat monoclonal antibody against α-tubulin YL1/2 (Pierce, MA1-80017, IF-1:600).

cDNAs. Mouse ASPM long isoform cDNA was purchased from Source Bioscience (OCACo5052D0620D). Fly Asp cDNA was provided by Drosophila Genomics Resource Center. Worm ASPM-1 cDNA was a gift of M. Boxem (Utrecht University, the Netherlands). Mouse katanin p60 and p80 cDNA were gifts of C. Janke (Institut Curie, Paris, France). Calmodulin cDNA was a gift of M. Mikhaylova (Centre for Molecular Neurobiology Hamburg, Germany).

Generation of stable cell lines. Both knockout and knock-in cell lines were generated using CRISPR-Cas9 technology[45]. ASPM and p80 knockout cells were generated by introducing a single double-strand break (DSB) within the MSP (major sperm protein) domain of ASPM (MSP: residue 37–134; DSB position: proline 70) and WD40 domain of p80 (WD40: residues 6–295; DSB position: threonine 73), respectively. The design of donor vector for AAVS1 site was based on the established methodology[46]. The targeting sequences and primers to amplify the 5′ and 3′ homology arms are listed in Supplementary Table 1. Cas9 and single guide RNA were expressed in PX459 (Addgene, #62988). Gibson assembly was used to assemble the pUC19 based GFP and strep-GFP donor plasmids.

To generate knockout and knock-in cell lines, cells were transfected with PX459 bearing the appropriate single guide RNA with or without donor sequence, and selected for 2 days with 2 µg ml^{-1} puromycin. Single cell cloning was performed by serial dilution on day 4–5 after withdrawing the drug selection.

To generate human katanin p80 Y571A mutant (Y574A in mouse) cell line in HeLa and U2OS, a ssDNA that harbours Y571A mutation was co-transfected with PX459 bearing single guide RNA (Supplementary Table 1). A silent mutation was also introduced to facilitate the initial screen for correct clones by restriction enzyme digestion analysis of genotyping PCR products. The presence of homozygous Y571A alleles was verified by Sanger sequencing.

For EB3-TagRFP and PA-GFP-α-tubulin double knock-in at the AAVS1 site, a single AAVS1 donor that contains two CMV expression cassettes was used.

For mCherry-α-tubulin knock-in at AAVS1 site in GFP-ASPM knock-in cells, an extra SA-2A-Blas-pA cassette was inserted between the 5′ homology arm and the CMV expression cassette in the AAVS1 donor. After withdrawing the puromycin selection for 1 day, cells were selected with 10 µg ml^{-1} blasticidin for 1 week without serial dilution.

Immunofluorescence cell staining. To label microtubules, cells were fixed with −20 °C methanol for 10 min and post-fixed in 4% formaldehyde in phosphate-buffered saline (PBS) for 10 min at RT. To co-label microtubules and CEP135, cells were fixed with 4% formaldehyde and 0.05% glutaraldehyde in MRB80 buffer (80 mM PIPES, 4 mM MgCl2 and 1 mM EGTA pH6.8). To label other proteins, cells were fixed with −20 °C methanol for 5 min. Cells were rinsed with 0.15% Triton X-100 in PBS; subsequent washing and labelling steps were carried out in PBS supplemented with 2% bovine serum albumin and 0.05% Tween-20. At the end, slides were rinsed in 70% and 100% ethanol, air-dried and mounted in Vectashield mounting medium (Vector Laboratories).

Protein expression and purification from HEK293T cells. To overexpress proteins in HEK293T cells, cDNAs were cloned into pEGFP-C1 (Takara) or pCoofy40 (ref. 47) (Addgene, #44006) based expression vectors.

To purify strep-GFP-ASPM short isoform/calmodulin, ASPM D1 fragment and fly Asp, 24 h post transfection, HEK293T cells were treated with 200 ng ml^{-1} nocodazole for 16 h before harvesting. The cells from one 15 cm dish were lysed in 900 µl lysis buffer (50 mM HEPES, 300 mM NaCl, 0.5% Triton X-100, pH 7.4) supplemented with protease inhibitors (Roche). After clearing debris by centrifugation, cell lysates were incubated with 100 µl StrepTactin beads (GE Healthcare) for 45 min. Beads were washed five times with lysis buffer without protease inhibitors and twice with wash buffer (50 mM HEPES, 150 mM NaCl, 0.05% Triton X-100 and 10% glycerol). The proteins were eluted in 60 µl elution buffer (50 mM HEPES, 150 mM NaCl, 0.05% Triton X-100, 10% glycerol and 2.5 mM desthiobiotin).

To purify other proteins, cells were collected after 36 h transfection without nocodazole treatment. 10% glycerol was omitted and 0.01% Triton X-100 instead of 0.05% Triton X-100 was used in the elution buffer.

To co-purify different katanin complexes, p80C with strep-SNAP or strep-GFP tag was co-transfected with p60 full length or fragments without any tags.

To label SNAP tagged proteins with Alexa647 dye (NEB), 20–40 µM dye was incubated with proteins on beads for 1 h between wash and elution steps. After extensive washing, proteins were eluted in the elution buffer with 300 mM instead of 150 mM NaCl.

All purified proteins were snap frozen in liquid nitrogen and stored in −80 °C.

Protein expression and purification from *E. coli*. To co-express p60 full length or p60N (AA 1-78) together with p80C (AA 481-658), the second gene with its own Shine–Dalgarno sequence was inserted after the stop codon of the first gene, so that the two proteins were expressed from the same promoter.

GST-p80C/p60N was expressed in the pGEX 6p-1 vector (GE Healthcare) and purified with Glutathione Sepharose 4 fast flow (GE Healthcare).

6xHis-p80C/p60N was expressed in the pET28a vector (Novagen). Bacterial cells were lysed by ultrasonication in a buffer containing 50 mM HEPES, pH 7.4, supplemented with 500 mM NaCl, 5 mM 2-mercaptoethanol and 10 mM imidazole. The complex was subsequently purified at 4 °C by IMAC on a 5 ml HisTrap FF Crude column (GE Healthcare) according to the manufacturer's instructions. The last purification step included size-exclusion chromatography on a Superdex 75 column in a buffer containing 20 mM HEPES, pH 7.4, supplemented with 150 mM NaCl.

A double tagging approach was used to purify GFP-p80C/p60 in *E. coli*. 6XHis-GFP-p80C/strep-p60 was expressed in pET28a based vector (Novagen). Following the first step purification by Ni-NTA agarose (Qiagen), proteins were eluted and purified again by StrepTactin beads (GE Healthcare). Elutions from StrepTactin beads were concentrated and run on a Superose 6 gel filtration column.

In all cases, *E. coli* BL21 (DE3) strain was used for expression. All purified proteins were snap frozen in liquid nitrogen and stored in −80 °C.

ASPM and TAMRA-labelled ASPM peptides were assembled on an automated continuous-flow synthesizer employing standard methods.

***In vitro* microtubule assays.** The *in vitro* assays with dynamic microtubules were performed under the same conditions as described previously[34]. Briefly, after functionalizing coverslips by sequentially incubating them with 0.2 mg ml^{-1} PLL-PEG-biotin (Susos AG, Switzerland) and 1 mg ml^{-1} neutravidin (Invitrogen) in MRB80 buffer, GMPCPP-stabilized microtubule seeds were attached to coverslips through biotin–neutravidin interactions. Flow chambers were further blocked with 1 mg ml^{-1} κ-casein. The reaction mix with purified proteins (MRB80 buffer supplemented with 20 µM porcine brain tubulin, 0.5 µM X-rhodamine-tubulin, 50 mM KCl, 1 mM GTP, 0.2 mg ml^{-1} κ-casein, 0.1% methylcellulose and oxygen scavenger mix (50 mM glucose, 400 µg ml^{-1} glucose oxidase, 200 µg ml^{-1} catalase and 4 mM DTT)) was added to the flow chamber after centrifugation. The flow chamber was sealed with vacuum grease, and dynamic microtubules were imaged immediately at 30 °C using a total internal reflection fluorescence (TIRF) microscope. When katanin proteins were used, 1 mM ATP was included in the reaction mix. In flow-in experiments, the reaction mix with purified proteins was flowed into an unsealed flow chamber with pre-assembled microtubules on stage. The conditions for severing assays with GMPCPP-stabilized microtubules were the same as in the assays with dynamic microtubules, except that tubulin was not included in the reaction mix. All tubulin products were from Cytoskeleton.

Image processing. Kymograph analysis and various quantifications were performed in ImageJ and MetaMorph. For measuring the velocity of the spindle flux, a low-pass filter and averaging between two consecutive frames were performed in MetaMorph to enhance the signal-to-noise ratio. An ImageJ macro was used to facilitate measurements of the distance between the photoactivated GFP-α-tubulin mark and the spindle pole. The pole position was defined by the centre of a circular region of interest (ROI) that enclosed the tubulin signal at the centrosome. After defining the two spindle pole positions, we measured the distance between the two poles. Polygon ROIs were used to define the photoactivated GFP-tubulin mark. Each pixel within Polygon ROIs was projected onto the line that connected the two spindle poles and the distance between the projected pixel and the pole was measured. By repeating this operation for all the pixels within ROIs, we got the average distance between photoactivated GFP-α-tubulin mark and the pole. The measurements were

DOI: 10.1038/ncb3511

performed at approximately 8–10 time points with an ~20–30 s interval. Linear regression was done with a built-in fitting function in ImageJ.

For measurement of ASPM and katanin intensities on dynamic microtubule minus ends, kymographs were first generated in ImageJ. The minus-end positions were marked by 5-pixel-wide linear ROIs corresponding to the ASPM signals. The maximum intensity within a 5-pixel region along the spatial axis of the kymograph was measured using a macro written in ImageJ.

To analyse the curvature of p60N+L/p80C decorated microtubules, we manually traced curved microtubules with ~10–15 points. The curvature was calculated by the LineCurvature2D function written in Matlab (MathWorks File Exchange: 2D Line Curvature and Normals). The function first fits polygons to the points, then calculates the analytical curvature from the polygons. The curvature at the breaking point was averaged over several time points before the appearance of a visible 'corner'.

Images were prepared for publication using ImageJ, MetaMorph and Adobe Photoshop.

Total internal reflection fluorescence (TIRF) microscopy. TIRF microscopy performed on an inverted research microscope Nikon Eclipse Ti-E (Nikon) with a perfect focus system (PFS) (Nikon), equipped with a Nikon CFI Apo TIRF 100 × 1.49 N.A. oil objective (Nikon), Photometrics Evolve 512 EMCCD (Roper Scientific) or CoolSNAP HQ2 CCD camera (Roper Scientific) and controlled with the MetaMorph 7.7 software (Molecular Devices). Images were projected onto the chip of an Evolve 512 camera with an intermediate lens 2.5× (Nikon C mount adapter 2.5×) or onto a CoolSNAP HQ2 without the lens. In both cases the final magnification was 0.063 μm pixel^{-1}. To keep cells at 37 °C or *in vitro* samples at 30 °C we used a stage top incubator INUBG2E-ZILCS (Tokai Hit).

For excitation lasers we used 491 nm 100 mW Stradus (Vortran), 561 nm 100 mW Jive (Cobolt) and 642 nm 110 mW Stradus (Vortran). We used an ET-GFP 49002 filter set (Chroma) for imaging of proteins tagged with GFP, an ET-mCherry 49008 filter set (Chroma) for imaging X-Rhodamine labelled tubulin or mCherry-EB3 and an ET-405/488/561/647 for imaging SNAP-Alexa647. For simultaneous imaging of green and red fluorescence, we used a triple-band TIRF polychroic ZT405/488/561rpc (Chroma) and a triple-band laser emission filter ZET405/488/561m (Chroma), mounted in a metal cube (Chroma, 91032) together with an Optosplit III beamsplitter (Cairn Research) equipped with a double-emission filter cube configured with ET525/50m, ET630/75m and T585LPXR (Chroma). We used sequential acquisition for triple-colour imaging experiments.

For photoablation experiments we used the same ILas system with the 532 nm Q-switched pulsed laser (Teem Photonics).

Spinning disk imaging. Spinning disk microscopy was performed on an inverted research microscope Nikon Eclipse Ti-E (Nikon) with a perfect focus system (PFS) (Nikon), equipped with a Plan Apo VC 100× N.A.1.40 oil objective (Nikon), CSU-X1-A1 Spinning Disc (Yokogawa) and Photometrics Evolve 512 EMCCD camera (Roper Scientific) and controlled with the MetaMorph 7.7 software (Molecular Devices). Images were projected onto the chip of an Evolve 512 camera with intermediate lens 2.4× (Edmund Optics) at a magnification of 0.066 μm pixel^{-1}. To keep cells at 37 °C we used a stage top incubator INUBG2E-ZILCS (Tokai Hit).

The microscope was equipped with a custom-ordered illuminator (Nikon, MEY10021) modified by Roper Scientific France/PICT-IBiSA, Institut Curie. 405 nm (100 mW) Stradus (Vortran), 491 nm (100 mW) Calypso (Cobolt) and 561 nm (100 mW) Jive (Cobolt) lasers were used for excitation or photoactivation. The spinning disk was equipped with a 405-491-561 triple-band mirror and GFP, mCherry and GFP/mCherry emission filters (Chroma).

For the photoablation experiments we used the same ILas system. A 355 nm passively Q-switched pulsed laser (Teem Photonics) was used for the photoablation together with the CFI S Fluor 100× 0.5-1.3 N.A. oil objective (Nikon).

Mass spectrometry. To identify ASPM binding proteins, endogenous strep-GFP-ASPM protein and its binding partners were pulled down by StrepTactin beads from HEK293T strep-GFP-ASPM knock-in cells, which were treated with 200 ng ml^{-1} nocodazole for 16 h before harvesting. To verify the purity of proteins used for *in vitro* assay, approximately 0.1–1 μg of purified proteins were subjected to mass spectrometry analysis. After in-gel digestion, samples were resuspended in 10% formic acid (FA)/5% DMSO and were analysed with an Agilent 1290 Infinity LC (Agilent Technologies), operating in reverse-phase (C18) mode, coupled to a TripleTOF 5600 (AB Sciex). MS spectra (350–1,250 *m/z*) were acquired in high-resolution mode (R > 30,000), whereas MS2 was in high-sensitivity mode (R > 15,000).

Raw files were processed using Proteome Discoverer 1.4 (version 1.4.0.288, Thermo Scientific). The database search was performed using Mascot (version 2.4.1, Matrix Science) against a Swiss-Prot database (taxonomy human). Carbamidomethylation of cysteines was set as a fixed modification and oxidation of methionine was set as a variable modification. Trypsin was specified as enzyme and up to two miscleavages were allowed. Data filtering was performed using percolator, resulting in 1% false discovery rate (FDR). Additional filters were; search engine rank 1 peptides and ion score >20.

Analytical ultracentrifugation. Sedimentation velocity experiments were performed using a ProteomeLab XL-I Beckman Coulter analytical ultracentrifuge equipped with an AN50Ti rotor. All measurements were conducted at 20 °C and at 42,000 r.p.m. in 20 mM HEPES, pH 7.4, supplemented with 150 mM NaCl, and 2 mM 2-mercaptoethanol. All data were collected at 280 or 555 nm using an absorbance optical system. Data analysis was performed with the SEDFIT software package[48] using a sedimentation coefficient distribution model c(s). Detection of the TAMRA-labelled ASPM peptide (ASPMp), residues 347–355 of mouse ASPM, was carried out at 555 nm. The binding curves describing the interaction between the TAMRA-labelled ASPMp and p60N/p80C complex were generated by integrating c(s) distributions. The fraction of ASPMp bound (FB) was calculated from the equation

$$FB = (A_{obs} - A_{min})/(A_{max} - A_{min}) \quad (1)$$

where A_{max} is the maximum area under the peak at saturating p60N/p80C protein complex concentrations, A_{obs} is the area under the peak for any p60N/p80C concentration, and A_{min} corresponds to the area under the peak in the absence of p60N/p80C. FB was plotted against the p60N/p80C protein concentration. The equilibrium dissociation constant, Kd, of the p60N/p80C/ASPM complex was obtained by fitting the data to the equation

$$FB = \left\{ Kd + P1 + P2 - \sqrt{(Kd + P1 + P2)^2 - 4P1P2} \right\} / 2$$

where P1 is the concentration of the TAMRA-labelled ASPM peptide and P2 is the concentration of the p60N/p80C complex. All fittings were performed using the ORIGIN software.

Circular dichroism spectroscopy. Far-ultraviolet (UV) circular dichroism spectra of wild-type and all the p60N/p80C complex mutants (5 μM) were obtained by scanning wavelengths from 200 nm to 260 nm using a Chirascan-Plus instrument (Applied Photophysics) equipped with a computer-controlled Peltier element. All experiments were performed in PBS. A ramping rate of 1 °C min^{-1} was used to record thermal unfolding profiles. Midpoints of the transitions, T_m, were taken as the maximum of the derivative $d[\theta]_{222}/dT$.

Crystallization and structure determination. The p60N/p80C/ASPMp (ASPMp: residues 347–355 of mouse ASPM) complex in 20 mM HEPES, pH 7.5, supplemented with 150 mM NaCl, was concentrated to 20 mg ml^{-1} prior to crystallization. Crystals of the complex grew within few hours at 20 °C in 20% PEG 3350, 0.1 M BisTris propane, pH 8.0, 0.2 M $NaNO_3$ using the sitting drop method. For cryo-protection, the reservoir solution was supplemented with 25% ethylene-glycol. The obtained crystals diffracted to 1.5 Å resolution. A complete dataset was acquired at the X06DA beamline of the Swiss Light Source at a wavelength of 0.9794 Å and 100 K temperature, and processed using XDS[49]. The structure was solved by molecular replacement in space group *C*222 using the p60N/p80C heterodimer structure (PDB ID 5NBT) as a search model. Structure refinement was carried out with Phenix.refine from the Phenix software suite[50]. COOT was used for manual rebuilding[51]. The refined p60N/p80C/ASPMp structure had 99.2% of residues in the most favoured Ramachandran plot region and no outliers, and a MolProbity score of 1.78. Data and refinement statistics are reported in Supplementary Table 3.

Statistics and reproducibility. Statistical comparison between the data from different groups was performed and the precise *P* values are calculated in Matlab (MathWorks) using the Rank Sum Test function (Mann–Whitney *U* test). All data shown are mean ± s.d. The sample size is indicated in the figure legends. All data presented in this study were either averages or representative data from at least two independent experiments, except the data related to mass spectrometry experiments (Fig. 1a and Supplementary Tables 2 and 4) and Sanger sequencing (Supplementary Fig. 2b). Images shown in Figs 1b, 3b–d,g–h, 4c–g, 5d,e, 6g,r, 7b–d, 8a and Supplementary Figs 1a, 2a, 3b, 5e–f, 6c–e,h,k are representative of two experiments. Images shown in Figs 1c–e, 2a,c,e, 5a–c,j–p, 6a–f,h,m–o, 7g,h–j, 8b–c,e,g,i and Supplementary Figs 1b, 2c–d,f–g, 4a–b, 5a–d, 6a–b, are representative of at least three experiments.

Code availability. The ImageJ Macros used in this study are available from the corresponding author on request.

Data availability. The structure of p60N/p80C/ASPMp was deposited in the PDB under accession code 5LB7. The protein interactions from this publication have been submitted to the IMEx (http://www.imexconsortium.org) consortium through IntAct[52] and assigned the identifier IM-25667. Statistical source data for Figs 1f, 2b,d,f, 5f–h, 6i–l,q, 7a–c,e–f,k,l, 8d,f,h,j and Supplementary Figs 2e and h–j, 6f–g, i–j, l–m, and the precise *P* values of Mann–Whitney *U* test can be found in Supplementary Table 5. All data that support the conclusions are available from the authors on reasonable request, and/or available in the manuscript itself.

45. Ran, F. A. *et al*. Genome engineering using the CRISPR-Cas9 system. *Nat. Protoc.* **8,** 2281–2308 (2013).
46. Hockemeyer, D. *et al*. Efficient targeting of expressed and silent genes in human ESCs and iPSCs using zinc-finger nucleases. *Nat. Biotechnol.* **27,** 851–857 (2009).
47. Scholz, J., Besir, H., Strasser, C. & Suppmann, S. A new method to customize protein expression vectors for fast, efficient and background free parallel cloning. *BMC Biotechnol.* **13,** 12 (2013).
48. Schuck, P. Size-distribution analysis of macromolecules by sedimentation velocity ultracentrifugation and lamm equation modeling. *Biophys. J.* **78,** 1606–1619 (2000).
49. Kabsch, W. Xds. *Acta Crystallogr. D Biol. Crystallogr.* **66,** 125–132 (2010).
50. Adams, P. D. PHENIX: a comprehensive Python-based system for macromolecular structure solution. *Acta Crystallogr. D Biol. Crystallogr.* **66,** 213–221 (2010).
51. Emsley, P., Lohkamp, B., Scott, W. G. & Cowtan, K. Features and development of Coot. *Acta Crystallogr. D Biol. Crystallogr.* **66,** 486–501 (2010).
52. Orchard, S. *et al*. The MIntAct project–IntAct as a common curation platform for 11 molecular interaction databases. *Nucleic Acids Res.* **42,** D358–D363 (2014).

Erratum: Microtubule minus-end regulation at spindle poles by an ASPM–katanin complex

Kai Jiang, Lenka Rezabkova, Shasha Hua, Qingyang Liu, Guido Capitani, A. F. Maarten Altelaar, Albert J. R. Heck, Richard A. Kammerer, Michel O. Steinmetz and Anna Akhmanova

Nature Cell Biology **19,** 480–492 (2017); published online 24 April 2017; corrected after print 22 May 2017

In the original version of this Article, the name of author A. F. Maarten Altelaar was coded wrongly, resulting in it being incorrect when exported to citation databases. This has now been corrected, though no visible changes will be apparent.

nature cell biology

DOI: 10.1038/ncb3511

In the format provided by the authors and unedited.

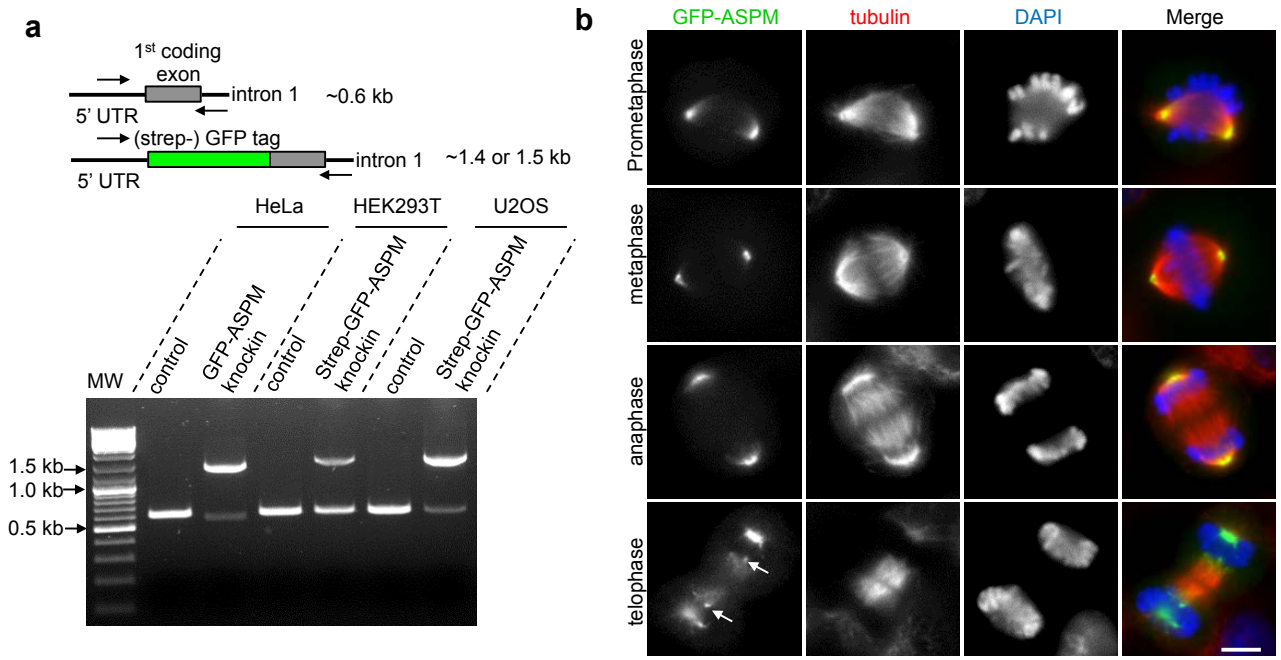

Supplementary Figure 1 Characterization of ASPM knock-in cell lines. **(a)** Genotyping of GFP and strep-GFP-ASPM knock-in cells used in this study. **(b)** Immunostaining for α-tubulin and DNA (DAPI) in GFP-ASPM knock-in HeLa cells during mitosis. White arrows indicate the localization of ASPM to the microtubule minus ends in the central spindle in telophase. Scale bar, 5 μm.

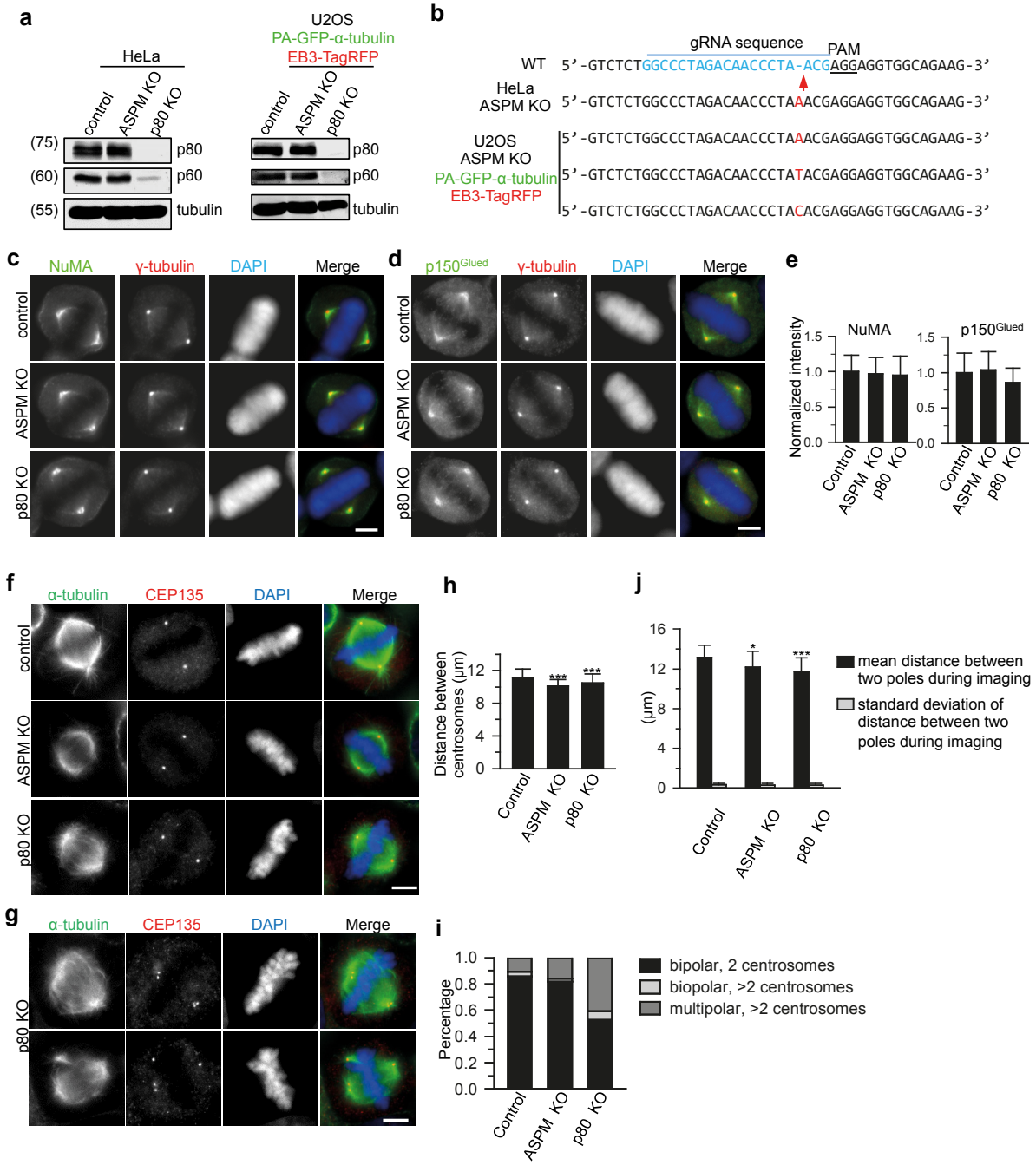

Supplementary Figure 2 ASPM and katanin regulate spindle architecture. **(a)** Western blotting with the indicated antibodies in control, ASPM knockout and p80 knockout cells (left, HeLa; right, U2OS PA-GFP-α-tubulin). Note that the knockout of p80 caused the concomitant loss of p60, in agreement with the fact that the two subunits form a tight complex. **(b)** Sequencing results of ASPM knockout cell lines used in this study. 1 nt insertion will result in p.N71KfsX31 or p.E72RfsX30. **(c-d)** Immunostaining of γ-tubulin, DNA (DAPI), and NuMA (c) or $p150^{Glued}$ (d) in control, ASPM knockout, and p80 knockout HeLa cells. Scale bar, 5 μm. In HeLa cells, the intensity of NuMA and $p150^{Glued}$ at the spindle pole remained largely unchanged in both ASPM and p80 knockout cells. **(e)** Quantification of spindle pole intensities of NuMA, and $p150^{Glued}$ as shown in panels c,d. For NuMA intensity, n=164 spindle poles, control; n=172, ASPM knockout; n=176, p80 knockout. For $p150^{Glued}$ intensity, n=160, control; n=166, ASPM knockout; n=170, p80 knockout. **(f,g)** Immunostaining for α-tubulin, CEP135 and DNA in control, ASPM knockout and p80 knockout HeLa cells (f, bipolar spindles with 2 centrosomes; g, bipolar and multipolar spindles with > 2 centrosomes in p80 knockout cells). Scale bar, 5 μm. **(h)** Quantification of the distance between two centrosomes in control, ASPM knockout and p80 knockout HeLa cells as shown in (f). n=67 cells, control; n=61, ASPM knockout, n=90, p80 knockout. **(i)** Quantification of centrosome numbers as shown in (f, g). 470 cells, control; 469, ASPM knockout; 572, p80 knockout (2 experiments). **(j)** Quantification of the average distance between two spindle poles in photoactivation experiments in U2OS cells as shown in Fig. 2e. n=26 cells, control; n=29, ASPM knockout; n=26, p80 knockout. The standard deviations of the distance between the two poles during imaging were small (~0.3 μm), which means that the spindle length kept constant during imaging. Compared to control, spindle length in ASPM and p80 knockout HeLa (h) and U2OS (j) cells shows 6~10% reduction. Data represent mean ± SD. *, P<0.05, ***, P<0.001, Mann-Whitney U test. Unprocessed original scans of blots are shown in Supplementary Figure 8. Source data for panels e, h, i and j can be found in Supplementary Table 5.

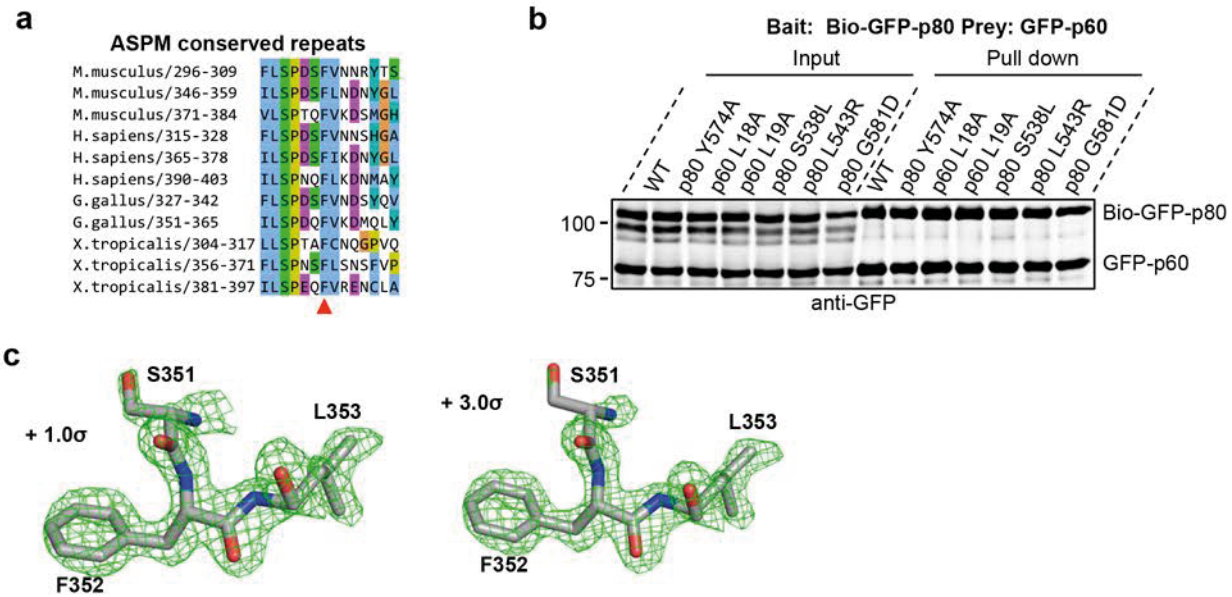

Supplementary Figure 3 The interaction between ASPM and katanin requires a conserved repeat sequence of ASPM and the p60N/p80C heterodimer. **(a)** Alignment of katanin-binding linear motifs of ASPM from several vertebrate species. Note the complete conservation of the phenylalanine residue corresponding to F352 in the third repeat of mouse ASPM (red arrowhead below the alignment). **(b)** Streptavidin pull down assays with extracts of HEK293T cells expressing Biotinylation tagged (Bio)-GFP-tagged wild type (WT) p80 or its indicated mutants together with GFP-tagged WT p60 or the indicated mutants. None of the analyzed mutations perturbed the p60-p80 interaction. See also Supplementary Fig. 8e. **(c)** Electron density maps of ASPMp in the p60N/p80C/ASPMp complex structure. Only residues S351, F352 and L353 of the ASPMp peptide (LSPDSFLND, residues 347-355 of mouse ASPM) are visible. The SigmaA-weighted 2mFo-DFc (left) and mFo-DFc (right) omit maps (green mash) are contoured at + 1.0σ and + 3.0σ, respectively.

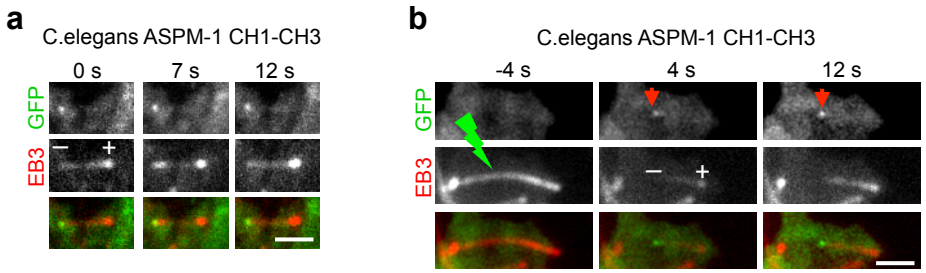

Supplementary Figure 4 The CH1-CH3 fragment of *C. elegans* ASPM-1 binds microtubule minus-end in cells. **(a,b)** The worm ASPM-1 CH1-CH3 fragment associates with minus ends of free microtubules (a) or minus ends freshly generated by photoablation (b) in interphase MRC5 cells. Green lightning bolts indicate the sites of photoablation. Scale bars, 2 μm.

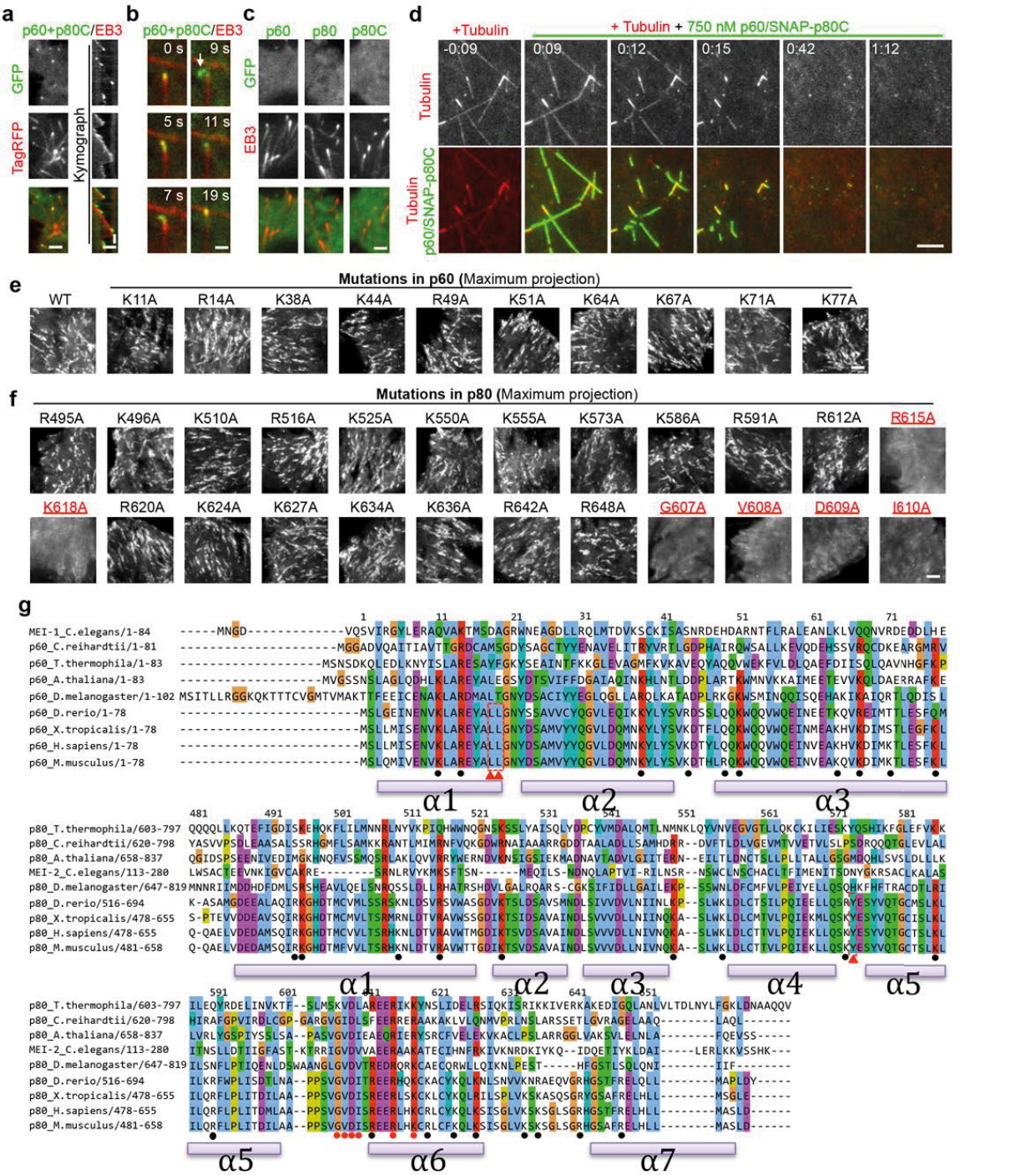

Supplementary Figure 5 The katanin p60/p80 heterodimer decorates and bends microtubule ends. **(a)** TIRFM live cell imaging and kymographs of colocalization of GFP-p60/p80C and EB3-TagRFP in MRC5 cells. Scale bars: horizontal, 2 µm; vertical, 10 sec. **(b)** Live cell images of a single microtubule plus end bound to GFP-p60/p80C and EB3-TagRFP in MRC5 cells. White arrow, breaking of a bent microtubule end. Scale bar, 1 µm. **(c)** Live imaging of MRC5 cells expressing individual katanin subunits together with EB3-TagRFP. Scale bar, 2 µm. **(d)** TIRFM time lapse images showing the complete severing of dynamic microtubules by p60/SNAP-Alexa647-p80C at 750 nM in a flow-in experiment. Time represented as min:sec. Scale bar, 2 µm. **(e-f)** Maximum intensity projections of time lapse images of GFP-p60/p80 WT or mutants in HeLa cells. Imaging was performed using TIRFM with 500 ms exposure in a stream mode. 100-200 images representing consecutive frames were used to make projections. Mutations of R615A, K618A, G607A, V608A, D609A and I610A in p80 completely abolish the end binding activity of p60/p80 in cells. Scale bar, 2 µm. **(g)** Protein sequence alignment of p60N and p80C from *Caenorhabditis elegans, Chlamydomonas reinhardtii, Tetrahymena thermophila, Arabidopsis thaliana, Drosophila melanogaster, Danio rerio, Xenopus tropicalis, Homo sapiens* and *Mus musculus*. The residues that are essential for microtubule end binding are indicated with red dots. Mutating charged residues denoted by black dots to alanine had no effect on end binding *in vivo*. Red triangles indicate the residues interacting with ASPM, which are conserved in vertebrates (red dashed rectangle). Numbers displayed on top of the sequence alignment are based on mouse katanin sequences.

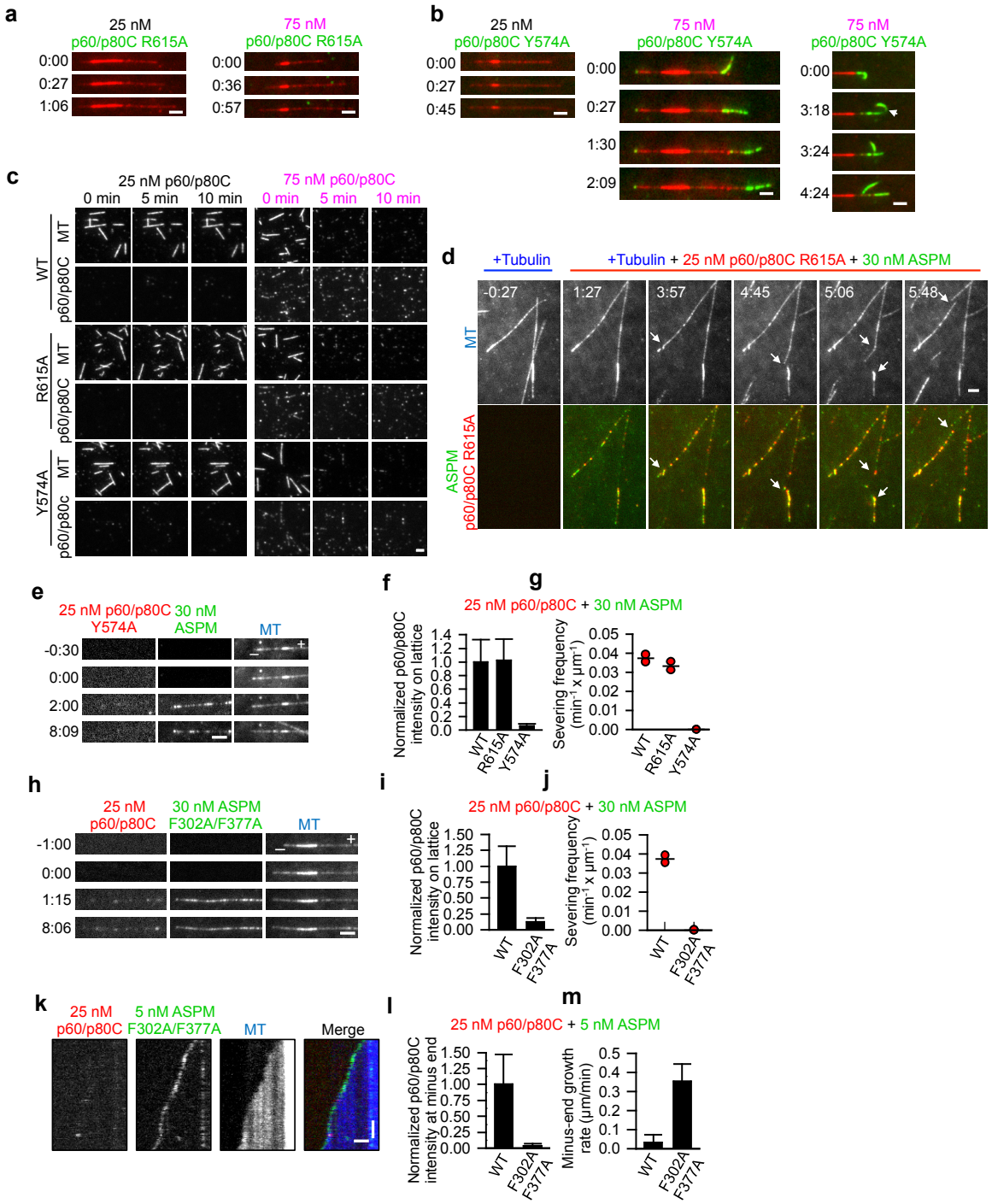

Supplementary Figure 6 Characterization of wild type katanin p60/p80C and its mutants, ASPM mutant and the ASPM/katanin complex at different concentrations. **(a)** The p60/p80C R615A mutant does not bind microtubule ends at 25 or 75 nM. Time represented as min:sec. Scale bars, 2 µm. **(b)** The p60/p80C Y574A mutant can decorate, bend and break microtubule ends at 75 nM but not at 25 nM. White arrow, breaking of a bent microtubule end. Time represented as min:sec. Scale bars, 2 µm. **(c)** Wild type (WT) p60/p80C and the indicated mutants can efficiently sever GMPCPP-stabilized microtubules at 75 nM but not at 25 nM. See Fig. 7a for quantification. Scale bar, 2 µm. **(d-g)** The p60/p80C R615A mutant but not the Y574A mutant at 25 nM can be recruited onto microtubule lattice and perform severing in the assay with dynamic microtubules in the presence of 30 nM ASPM. White arrows indicate the sites where severing events occur. Time represented as min:sec. **f**, n=64 (WT), 59 (R615A) and 59 (Y574A) microtubules; **g**, Data are the mean of 2 experiments. Scale bar, 2 µm. **(h-j)** 30 nM ASPM F302A/F377A mutant does not recruit p60/p80C to microtubule lattice and does not promote severing. **i**, n=62 (WT) and 60 (F302A/F377A) microtubules; **j**, data are the mean of 2 experiments. Severing frequency data for WT in panels g and j were replotted from Fig. 7f (30 nM). **(k-m)** 5 nM ASPM F302A/F377A mutant does not recruit p60/p80C to dynamic microtubule minus ends and does not induce their blocking. **l**, n=19 (WT) and 29 (F302A/F377A) microtubules; **m**, n=19 (WT) and 33 (F302A/F377A) microtubules. Scale bars, horizontal, 2 µm; vertical, 1 min. Data represent mean ± SD. Source data for panels f, g, i, j, l and m can be found in Supplementary Table 5.

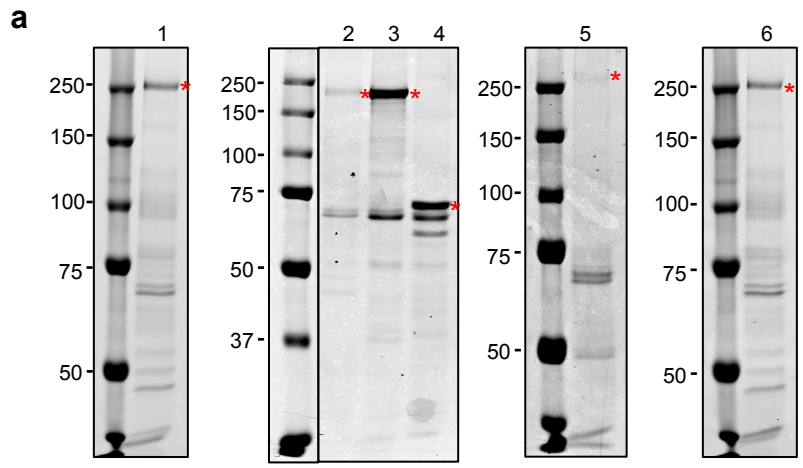

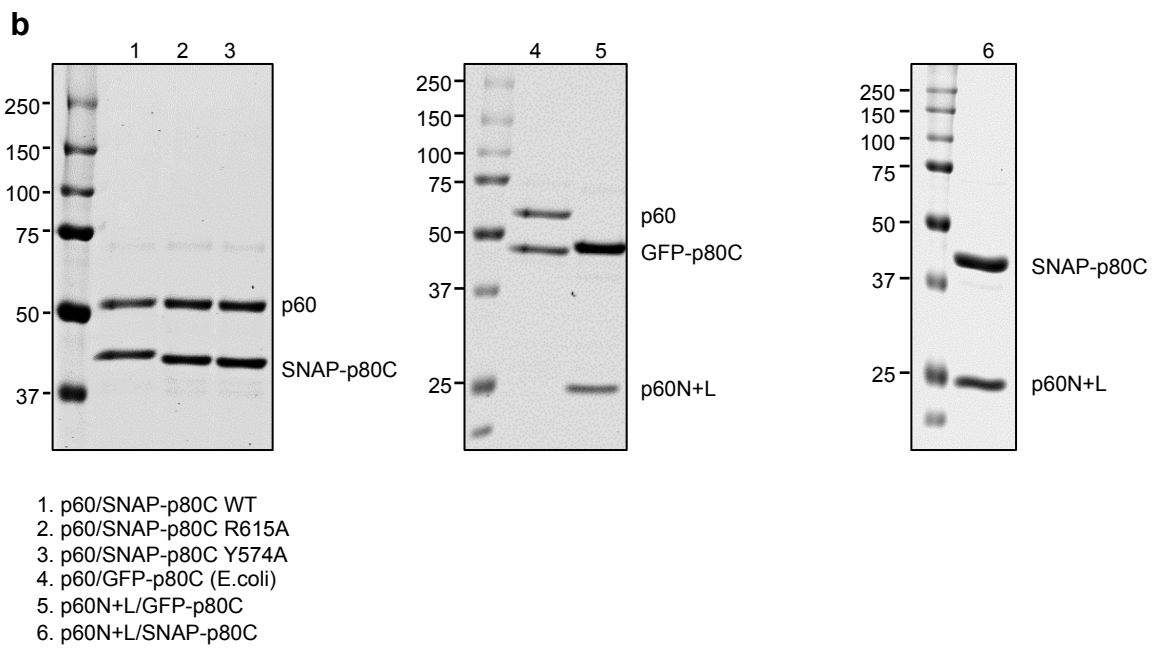

Supplementary Figure 7 Purified proteins used for *in vitro* reconstitution experiments. **(a)** Coomassie blue stained gels with strep-GFP tagged ASPM, Asp and ASPM-1 proteins purified from transiently transfected HEK293T cells. The bands corresponding to purified full length proteins are marked with red asterisks. **(b)** Coomassie blue stained gels with p60/strep-SNAP-p80C wild type and mutants, p60N+L/strep-GFP-p80C and p60N+L/strep-SNAP-p80C purified from HEK293T cells and strep-p60/6xHis-GFP-p80C purified from *E. coli*.

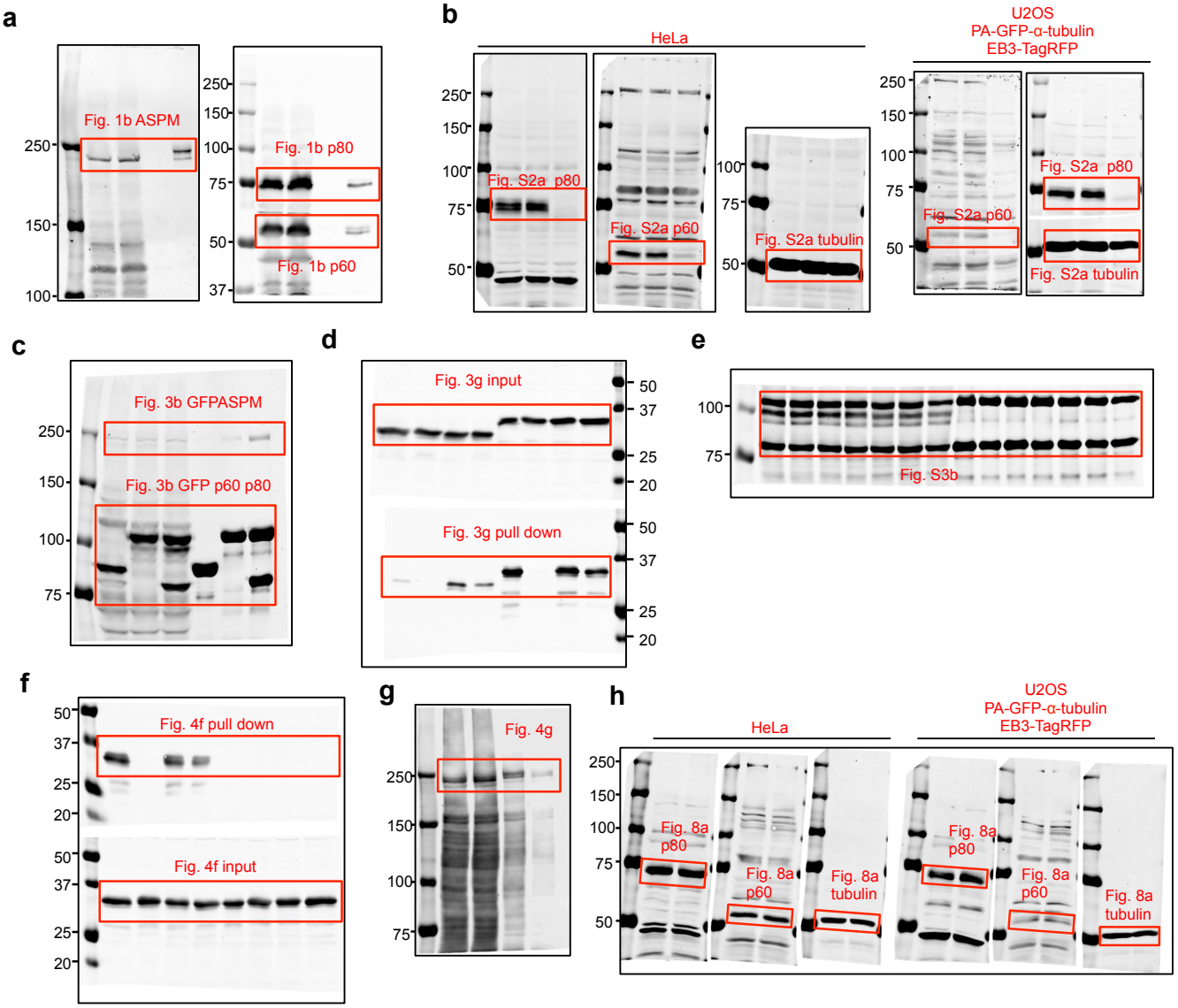

Supplementary Figure 8 Full scans of Western blots used to prepare figures, as indicated.

Supplementary Table Legends

Supplementary Table 1 CRISPR-Cas9 gRNA targeting sequences and PCR primers used for generating homology recombination donor constructs and genotyping.

Supplementary Table 2 List of proteins identified by mass spectrometry in the pull down of endogenously tagged strep-GFP-ASPM. StrepTactin pull down was performed from strep-GFP-ASPM knock-in HEK293T cells synchronized in mitosis. Purified endogenous ASPM protein and its binding partners were analyzed by mass spectrometry. Proteins identified after filtering out the background are shown.

Supplementary Table 3 Crystallographic data collection and refinement statistics.

Supplementary Table 4 Analysis of the proteins used for in vitro assays by mass spectrometry. Approximately 0.1-1 μg of purified proteins were subjected to mass spectrometry analysis. The hits with a score above 50 are shown. We noticed that p60 subunit A-like 1 was identified in purified katanin proteins from HEK293T cells. However, this is most likely due to sequence homology between p60 and p60 A-like 1, as p60 A-like 1 was also identified in *E.coli*-purified p60/GFP-p80C protein with a similar score.

Supplementary Table 5 Statistics Source Data. Statistical source data for Fig. 1f, 2b, 2d, 2f, 5f-h, 6i-l, 6q, 7a-c, 7e-f, 7k, 7l, 8d, 8f, 8h, 8j and Supplementary Fig. 2e, 2h-j, 6f-g, 6i-j, 6l-m, and the precise p values of Mann-Whitney U test.

Supplementary Video Legends

Supplementary Video 1 Reduced spindle flux in ASPM and katanin knockout cells. Photoactivation of PA-GFP-α-tubulin in control (left), ASPM knockout (middle) and katanin knockout (right) U2OS metaphase cells. Images were collected using a spinning disk microscope at 2 s interval. Video is sped up 60 times. Time is shown in the format min:sec.

Supplementary Video 2 Overexpressed katanin p60/p80 complex tracks and bends microtubule ends in cells. MRC5 cells were co-transfected with GFP-p60, p80 (dark) and EB3-TagRFP. Images were collected using a TIRF microscope in stream mode (2 frames/s). Video is sped up 15 times. Time is shown in the format min:sec.

Supplementary Video 3 Katanin p60/p80C severs dynamic microtubules at 300 nM *in vitro*. Microtubules were first polymerized in the tubulin polymerization reaction mix (20 μM unlabeled tubulin and 0.5 μM X-rhodamine-tubulin in MRB80 buffer supplemented with 50 mM KCl). Subsequently, the tubulin polymerization reaction mix supplemented with 300 nM p60/SNAP-Alexa647-p80C and 1 mM ATP was flowed into the reaction chamber. Images were collected using a TIRF microscope at a 3 s interval. Video is sped up 15 times. Time is shown in the format min:sec.

Supplementary Video 4 Katanin p60N+L/p80C bends and breaks a microtubule end *in vitro*. Microtubules were polymerized in the presence of 1 μM p60N+L/GFP-p80C, 20 μM unlabeled tubulin and 0.5 μM X-rhodamine-tubulin in MRB80 buffer supplemented with 50 mM KCl. Images were collected using a TIRF microscope at 2 s interval. Video is sped up 30 times. Time is shown in the format min:sec.

Supplementary Video 5 30 nM ASPM and 25 nM katanin p60/p80C sever dynamic microtubules *in vitro*. Microtubules were first polymerized in the tubulin polymerization reaction mix (20 μM unlabeled tubulin and 0.5 μM X-rhodamine-tubulin in MRB80 buffer supplemented with 50 mM KCl). Subsequently, tubulin polymerization reaction mix supplemented with 30 nM ASPM, 25 nM p60/SNAP-Alexa647-p80C and 1 mM ATP was flowed into the reaction chamber. Images were collected using a TIRF microscope at a 3 s interval. Video is sped up 15 times. Time is shown in the format min:sec.